buildings

MDPI

Article

Novel Acid-Resistant Hybrid Mortar with Calcium Sulfoaluminate and Zeolite for Impressed Current Cathodic Protection of Bridge Infrastructure

Hamid Fatemi [1], S. Ali Hadigheh [1,*], Georgius Adam [2], Shamila Salek [3], Qingtao Huang [3], Michael McKinnon [2] and Yunyun Tao [1]

[1] School of Civil Engineering, Faculty of Engineering, The University of Sydney, Sydney, NSW 2006, Australia; hamid.fatemi@sydney.edu.au (H.F.); yunyun.tao@sydney.edu.au (Y.T.)
[2] Parchem for Construction Supplies, Dulux Group Pty Ltd., Wyong, NSW 2259, Australia; georgius.adam@fosroc.com.au (G.A.); michael.mckinnon@fosroc.com.au (M.M.)
[3] Centre for Infrastructure Engineering, Western Sydney University, Sydney, NSW 2751, Australia; s.salek@westwrnsydney.edu.au (S.S.); qungtao.huang@westernsydney.edu.au (Q.H.)
* Correspondence: ali.hadigheh@sydney.edu.au

Abstract

Impressed current cathodic protection (ICCP) systems can experience acidification, which deteriorates the interface between the anode and the anode backfill mortar. This deterioration may necessitate premature intervention to remove and reinstate the backfill and, in some cases, replace the anode. If left unaddressed, acidification ultimately leads to debonding between the anode and the backfill mortar, resulting in the failure of the ICCP system. This paper presents the development of a specialised acid-resistant hybrid mortar designed for ICCP systems used to protect reinforced concrete bridges in marine environments. It also investigates the effects of acidification on the physical and mechanical properties of the proposed anode backfill mortars. Additionally, the study characterises acidification products from both field-extracted ICCP systems and laboratory-based accelerated testing, providing deeper insights into the acidification mechanisms. Novel mortar samples were subjected to varying concentrations of hydrochloric acid (HCl) under accelerated testing conditions. The incorporation of supplementary cementitious materials (SCMs), calcium sulfoaluminate (CSA) cement and zeolite significantly enhanced the strength and durability of the backfill mortars in acidic environments, while maintaining compliance with the electrical resistivity requirements (20–100 kΩ·cm) for ICCP systems. The lowest compressive strength loss observed in the developed hybrid mortar was 54% after 28 days of immersion in 5% HCl and 83% in 15% HCl. Microstructural analyses revealed that gypsum formation and chloride–sulphate competitive binding interactions are key mechanisms contributing to the improved acid resistance, particularly in CSA cement-containing formulations.

Keywords: impressed current cathodic protection (ICCP); hybrid backfill mortar; supplementary cementitious materials (SCMs); calcium sulfoaluminate (CSA); acidification

Check for updates

Academic Editor: Junjie Zeng

Received: 11 November 2025
Revised: 12 December 2025
Accepted: 18 December 2025
Published: 22 December 2025

Copyright: © 2025 by the authors. Licensee MDPI, Basel, Switzerland. This article is an open access article distributed under the terms and conditions of the Creative Commons Attribution (CC BY) license.

1. Introduction

The corrosion-induced degradation of reinforced concrete is a significant durability concern for civil engineering structures exposed to marine environments, primarily due to the high concentration of chloride ions [1,2]. Among the various deterioration mechanisms, the corrosion of embedded steel reinforcement is particularly noteworthy. A range of

technologies, including material restoration, electrochemical treatments, surface protection, structural strengthening, and crack repair, have been adopted to mitigate chloride-induced deterioration in coastal infrastructures [3–5]. Among these, impressed current cathodic protection (ICCP) has emerged as a highly efficient technique for preventing corrosion in reinforced concrete, particularly in marine settings [6,7]. Hou et al. [8] reported that ICCP systems can reduce steel reinforcement corrosion by up to 67%.

The first application of ICCP for corrosion control in reinforced concrete took place in 1973 on a highway bridge in California, United States [9]. The technique involves applying an external current, known as an impressed current, to polarise the steel reinforcement towards more negative potentials, typically aiming to shift the steel potentials to a more cathodic state than −850 mV saturated calomel electrode (SCE), where the occurrence of corrosion is thermodynamically suppressed [10]. Under these conditions, the steel becomes effectively immune to corrosion [11].

A typical ICCP system consists of three main components: an external direct current (DC) power supply, the cathode (the embedded steel reinforcement), and an anode system [1,12,13]. The anode system commonly comprises a noble mesh or ribbon connected to an external DC power supply, delivering current through an anode backfill mortar to the steel reinforcement embedded in concrete, which functions as the electrolyte [14]. Mixed metal oxide-coated titanium (MMO/Ti) is widely used as the anode material due to its high current capacity and stability [12,15]. The anode is embedded and surrounded by a conductive backfill mortar, which serves as an ionic medium facilitating current flow between the anodes and the adjacent concrete [1,12]. Despite its important role within the ICCP systems, the durability of anode backfill mortar, particularly its susceptibility to acidification, has increasingly been recognised as a limiting factor governing the long-term performance and reliability of ICCP in reinforced concrete structures [13].

During the ICCP treatment, a typical DC density of up to 110 mA/m^2 is applied between the anode and the cathode using an external power supply, causing the protection current to flow through the concrete as the electrolyte [16]. At the cathode, the steel reinforcement surface becomes negatively polarised, repelling chloride ions (Cl^-). Simultaneously, cathodic reduction reactions consume dissolved oxygen (O_2) and water (H_2O) according to the following electrochemical reactions [11,17]:

$$O_2 + 2H_2O + 4e^- \rightarrow 4OH^- \quad (1)$$

$$2H_2O + 2e^- \rightarrow H_2 + 2OH^- \quad (2)$$

These reactions generate hydroxyl ions (OH^-) at the steel surface, increasing the local pH and facilitating re-passivation of the reinforcement [17].

At the anode, oxidation reactions occur at the interface between the anode and the backfill mortar, continuously consuming OH^- from the pore solution. In the presence of Cl^-, chlorine gas is formed and subsequently reacts with water to produce hypochlorous acid (HClO) and hydrochloric acid (HCl) at the anode surface [1,17]:

$$4OH^- \rightarrow 2H_2O + O_2 + 4e^- \quad (3)$$

$$2H_2O \rightarrow O_2 + 4H^+ + 4e^- \quad (4)$$

$$2Cl^- \rightarrow Cl_2 + 2e^- \quad (5)$$

$$Cl_2 + H_2O \rightarrow HClO + HCl \quad (6)$$

The sustained depletion of OH^- and the formation of acidic species lowers the pH in the pore solution, leading to dissolution of cement hydration products such as calcium hydroxide ($Ca(OH)_2$) and calcium silica hydrate (C-S-H) within the matrix [18,19]. HCl

progressively neutralised the cement matrix, forming soluble calcium chloride ($CaCl_2$) salt and water [20]. These reactions ultimately leave behind a silica gel residue:

$$Ca(OH)_2 + 2HCl \rightarrow CaCl_2 + 2H_2O \quad (7)$$

$$C\text{-}S\text{-}H + 2HCl \rightarrow CaCl_2 + Si(OH)_4 + H_2O \quad (8)$$

This degradation process increases microstructural porosity and reduces adhesion at the interface between the anode and the backfill mortar. This phenomenon, commonly referred to as acidification, compromises the durability of the anode system [18,19]. Additionally, the acidification process damages the anode surface and affects the conductivity of the backfill mortar, negatively affecting the uniform distribution of the protection current [18]. Prolonged acidification eventually leads to debonding between the anode and the backfill mortar, ultimately resulting in ICCP system failure [1,21]. Therefore, it is particularly important to use acid-resistant mortars in the ICCP system to prevent acidification.

In response to the growing awareness that anode backfill mortar degradation can critically limit the long-term effectiveness of ICCP systems, blended cements, known for their durability and acid resistance, are increasingly being considered as a potential solution. This approach not only addresses chemical degradation but also targets permeability and resistivity issues inherent to conventional mortars. Blended cement is a combination of ordinary Portland cement (OPC) and supplementary cementitious materials (SCMs), such as fly ash (FA), ground granulated blast-furnace slag (GGBS), or silica fume (SF), which are used as partial replacements for cement clinker [22]. Globally, blended cements have been widely adopted for several decades as an environmentally friendly solution that reduces greenhouse gas emissions while enhancing concrete durability [23,24].

Several studies have demonstrated the benefits of SCM incorporation. Mlinárik and Kopecskó [25] reported that adding 10–17% of SCMs reduced the chloride migration coefficient and permeable porosity, with samples exhibiting excellent resistance to sulphuric acid (mass loss < 4% after one year) compared to 10% for the reference cement sample. Similarly, Saraswathy and Song [26] investigated reinforced concrete slabs containing a 25% fly ash cement mixture under accelerated exposure to 3% NaCl and found that fly ash improved corrosion resistance, delayed the initial corrosion, and reduced corrosion rates in both cracked and uncracked concrete. The corrosion rate of steel reinforcement is closely linked to concrete resistivity, with high resistivity corresponding to lower corrosion rates [27]. Le et al. [27] reported that samples containing 10–30% SCMs (FA and GGBS) exhibited relatively high resistivity (98.3 to 98.5 kΩ.cm), while Wang et al. [28] found that samples with 20% SCMs (FA, GGBS, SF) exceeded 100 kΩ·cm, in contrast to 12–19 kΩ·cm for pure OPC samples [29,30].

While SCMs improve durability and resistivity, recent studies [31–33] have highlighted that further enhancements are possible through the incorporation of calcium sulfoaluminate (CSA) cement and zeolite. CSA-based binders contain little to no portlandite ($Ca(OH)_2$), the phase most susceptible to acidic attack, and form stable hydration products such as ettringite (AFt) and aluminium hydroxide ($Al(OH)_3$) [32,34]. Zeolite, a natural microporous aluminosilicate, exhibits strong pozzolanic activity and reacts with $Ca(OH)_2$ to form additional C-S-H and calcium aluminate compounds, refining the pore structure and improving long-term durability [33]. Its high specific surface area and open crystal structure also help reduce free water separation, enhancing workability in fresh concrete. When combined with CSA cement and SCMs, zeolite further mitigates capillary porosity, reduces calcium leaching and chloride penetration, and strengthens resistance to acid attack [32,33]. Collectively, these components form a hybrid synergistic system that not only improves mechanical and durability performance but also provides a promising approach for developing acid-resistant mortars suitable for ICCP backfill applications.

In addition to these blended cement systems, geopolymer and alkali-activated mortars are also well recognised for their superior resistance to hydrochloric and sulphuric (H_2SO_4) acid attack compared with OPC [35–37]. Their aluminosilicate gel network (typically N-A-S-H) contains no $Ca(OH)_2$ and C-S-H phases, and fewer calcium-rich phases, which reduces dissolution and decalcification under acidic conditions [35,38]. Vafaei et al. [39] reported that geopolymers exhibit significantly higher durability, showing only 3% and 29% mass change and 1% and 64% strength decline after exposure to HCl and H_2SO_4 solutions (pH = 3) at room temperature for 24 months. Despite this chemical durability, conventional geopolymers inherently exhibit very high electrical resistivity, for example, 6157.5 kΩ·cm after 28 days of curing, measured at 0.01 mA and 100 mm electrode spacing [40]. While such high resistivity is advantageous in structural and durability applications, it is a critical limitation for ICCP systems, where the anode backfill mortar must provide sufficient ionic conductivity to support stable current flow. Therefore, although geopolymer binders offer excellent acid resistance, their high electrical resistivity makes them unsuitable for anode backfill mortars in ICCP applications.

In the context of the ICCP system, the anode backfill mortar must achieve a balance between conductivity, low permeability, and high acid resistance to mitigate the risk of acidification. Australian Standard (AS) 2832.5 [16] specifies a maximum allowable resistivity of 100 kΩ.cm. By meeting these criteria, adverse effects from anodic electrochemical reactions can be effectively curtailed. However, despite the known benefits of blended cements and CSA/zeolite systems, the influence of acidification and electrical conductivity of backfill mortar on its efficacy within ICCP applications remains largely unexplored in the literature.

This paper aims to develop hybrid mortars for ICCP anode backfill material and assess their performance under conditions that simulate acidification-induced deterioration. In the first phase of the research, the effectiveness of an accelerated laboratory testing regime based on HCl immersion was assessed by comparing controlled laboratory samples with field-exposed backfill mortar extracted from an operational ICCP system on a bridge located in a coastal region in Australia. This validation provides a basis for the second phase of the study, in which novel hybrid mortars are developed and evaluated for improved acid resistance to the ICCP-related acidification. The experimental testing of hybrid backfill mortars to analyse the impact of ICCP acidification involves exposure to different concentrations of HCl solutions under an accelerated testing regime. The property evaluation also includes mechanical testing and microstructural analyses, including compressive strength, scanning electron microscopy (SEM), X-ray diffraction (XRD) and X-ray mapping (XRM), which will be performed to examine the acidified samples under both laboratory and real-world conditions. Additionally, resistivity measurements will be taken to determine the electrical conductivity of the hybrid backfill mortars and evaluate their suitability for ICCP application.

2. Experimental Programme

The experimental programme is designed to investigate the deterioration mechanisms of anode backfill mortars under acidification-induced degradation in ICCP systems, validate the accelerated HCl testing regime as a simulation of real-world acidification, and, most importantly, develop novel hybrid backfill mortars for acid resistance.

2.1. Simulating ICCP Acidification Using HCl

2.1.1. Field-Exposed and Controlled Laboratory Mortars

The in situ ICCP acidification study was undertaken on a bridge, constructed around 1989, located about 130 km north of Sydney, New South Wales, Australia [41]. It is located

adjacent to an older bridge, constructed in 1955 and, while similar in many respects to its predecessor, incorporates an opening span to accommodate large vessels [42]. Due to prolonged exposure to an aggressive marine environment, the bridge's substructure has experienced reinforcement corrosion. To mitigate this issue and extend the bridge's service life, a comprehensive ICCP system was implemented [41]. However, the bridge backfill mortar has deteriorated due to acidification at the anode, as shown in Figure 1. This acidification can compromise the durability of the ICCP system, leading to the spalling of the anode backfill mortar due to loss of the backfill mortar's binding capacity [43].



Figure 1. Images of the bridge pier show the deteriorated anode backfill mortar due to ICCP acidification.

To better understand the acidification mechanism, two deteriorated backfill mortar samples were collected from the bridge pier (areas A1 and A2, as shown in Figure 1). These field-exposed samples served as references, representing real-world ICCP-induced acidification damage. For direct comparison, controlled laboratory samples were prepared using HB-40, a Portland cement-based repair mortar of the same type originally used as ICCP backfill in the bridge pier. This material, commonly used with galvanic and ICCP anodes, contains 30–60 wt.% OPC, 30–60 wt.% quartz sand, and less than 5 wt.% calcium oxide, along with small amounts of organic and inorganic additives, including calcium formate and neopentyl glycol. The mortar typically achieves a 28-day compressive strength of 45.0 MPa. Laboratory specimens were cast into 70 mm cubes for subsequent accelerated acidification exposure.

2.1.2. Simulated Acidification with HCl Immersion

To develop an accelerated laboratory testing regime, 70 mm cubic laboratory samples were prepared and immersed in 10% and 32.5% HCl solutions (by weight). This was designed to simulate the ICCP-induced acidification process under controlled laboratory conditions [13,38]. After 28 days of standard moist curing, the cured cube samples were fully immersed in individual containers made of heavy-duty acid-resistant polypropylene. These containers were maintained at a constant temperature of 23 °C and 50% relative humidity for an additional 28-day exposure period. The concentration of the acid baths was checked weekly by titration against a standard 0.5 N potassium hydroxide solution using a phenolphthalein indicator. Adjustments were made to maintain the desired concentration.

Following exposure, microstructural and compositional analyses were conducted on both laboratory-exposed and field-collected samples to evaluate the extent of degradation and to assess the validity of the accelerated HCl immersion regime in simulating ICCP-induced deterioration observed in service.

2.1.3. Microstructural and Compositional Analyses

Powder XRD measurements were conducted on the backfill mortars using a Bruker D8 Advance Diffractometer (Karlsruhe, Germany) with CuKα radiation (λ = 1.5406 Å), LYNXEYE XE detector (Karlsruhe, Germany), and Bragg–Brentano geometry. The samples were examined in the 2θ ranges of 5° to 90° with a time/step of 2 s. The phases were identified using the Bruker EVA software and XRD data from the International Centre for Diffraction Data (ICDD) Powder Diffraction File (PDF) database.

SEM-EDS analyses were performed using a Hitachi FlexSEM II SEM (Tokyo, Japan) with a Bruker QUANTAX EDS system. Spectra were collected in a low vacuum (30 Pa) at an accelerating voltage of 20 keV and analysed using Bruker ESPRIT Compact software.

XRM was performed using a JEOL JSM-7001F (Jeol, Tokyo, Japan) field emission gun (FEG)-SEM equipped with Moran Scientific microanalysis system (Moran Scientific, Adelaide, Australia) and an Amptek silicon drift detector (SDD) (Amptek, Bedford, MA, USA) with a C2 (40 nm Si_3N_4) window. The map was collected in a high vacuum at an accelerating voltage of 15 keV. To conduct the XRM analysis, the sample was sectioned, resin impregnated, polished (up to 1 μm surface fineness), and carbon coated.

2.2. Development and Evaluation of New Hybrid Backfill Mortars

To mitigate the acidification-related deterioration observed in anode backfill mortars under ICCP systems, novel hybrid backfill mortars were developed in this study. These mortars are designed to offer enhanced resistance to acidic environments, aiming to prolong the service life and effectiveness of ICCP systems.

Based on the validated laboratory immersion regime using HCl solution, a comprehensive experimental programme was developed to investigate the behaviour of the hybrid backfill mortars under accelerated acidification conditions. The mortars were exposed to different HCl concentrations to assess their mechanical and microstructural performance in simulated ICCP-induced environments. This section details the materials used and the sample preparation, followed by an overview of the experimental methods employed to measure resistivity, mechanical and physical properties, as well as material characteristics.

2.2.1. Materials and Sample Preparation

Three different types of hybrid backfill mortars, HP-1, HP-2 and HP-3, were developed for accelerated testing. As shown in Table 1, HP-1 (A to D), HP-2 (A to D), and HP-3 (A to D) mixes were specifically designed for shotcrete, hand-applied and machine-pumping applications, respectively. The materials used in these mortars included OPC, SCMs, CSA cement, sodium aluminosilicate (zeolite) and quartz sand. OPC, GGBF and FA were supplied by Cement Australia; SF was supplied by Simcoa, Australia; CSA cement and zeolite were supplied by Bisley, Australia; and quartz sand was supplied by Sibelco, Australia. These mortars contained 19–31 wt.% OPC and 5–14 wt.% SCMs, such as GGBS, FA and SF. The incorporation of SCMs in the backfill mortars aimed to enhance their resistance to acidification damage caused by the ICCP system, as the ability of concretes containing SCMs to withstand deterioration in corrosive environments has been recognised [25,38].

Compared with the HP-1 group, the HP-2 and HP-3 groups included 3.3 wt.% and 2.5 wt.% CSA cement, respectively. The addition of CSA cement to HP-2 and HP-3 groups served to reduce setting time and improve early strength, mitigating the adverse effects of high-water content. Furthermore, the HP-2 group incorporated 4.7 wt.% zeolite to minimise water separation and enhance workability [33]. The water-to-binder ratio (w/b) for the HP-1, HP-2 and HP-3 groups was 0.39, 0.31 and 0.33, respectively. A total of twelve mortar

mixes were prepared in this study to compare the anti-acid effects of different proportions of OPC and SCMs. Detailed information regarding the mixing ratios is listed in Table 1.

Table 1. Backfill mortar mix proportions.

Mix ID	*w/b*	OPC wt.%	GGBS & FA wt.%	SF wt.%	CSA wt.%	Zeolite wt.%	Calcium Oxide wt.%	Quartz Sand wt.%
HB-40 *	0.31	30–60	–	–	–	–	<5	30–60
HB-40 Plus *	0.31	≤20	25–40	–	–	–	<5	30–60
HP-1A	0.39	22	3.5	1.5	–	–	–	73
HP-1B	0.39	21	4.5	1.5	–	–	–	73
HP-1C	0.39	20	5.5	1.5	–	–	–	73
HP-1D	0.39	19	6.5	1.5	–	–	–	73
HP-2A	0.31	31	11	–	3.3	4.7	–	50
HP-2B	0.31	30	12	–	3.3	4.7	–	50
HP-2C	0.31	29	13	–	3.3	4.7	–	50
HP-2D	0.31	28	14	–	3.3	4.7	–	50
HP-3A	0.33	24	6.5	0.5	2.5	–	–	66.5
HP-3B	0.33	23	7.5	0.5	2.5	–	–	66.5
HP-3C	0.33	22	8.5	0.5	2.5	–	–	66.5
HP-3D	0.33	21	9.5	0.5	2.5	–	–	66.5

* Proprietary reference mortars. *w*/*b*: water to binder ratio.

The mortars were mixed according to the manufacturer's instructions and standard mixing procedures [44]. After mixing, the fresh mortar was cast into 100 mm × 200 mm cylindrical moulds for surface resistivity testing and 70 mm cubic moulds for acid-resistant evaluation at various ages. The samples remained in the moulds for 24 h before being demoulded and placed under standard moist-curing conditions as specified in AS 1012.8.3 [45]. Figure 2 shows the hybrid backfill mortar samples prepared for the acid-resistant evaluation.

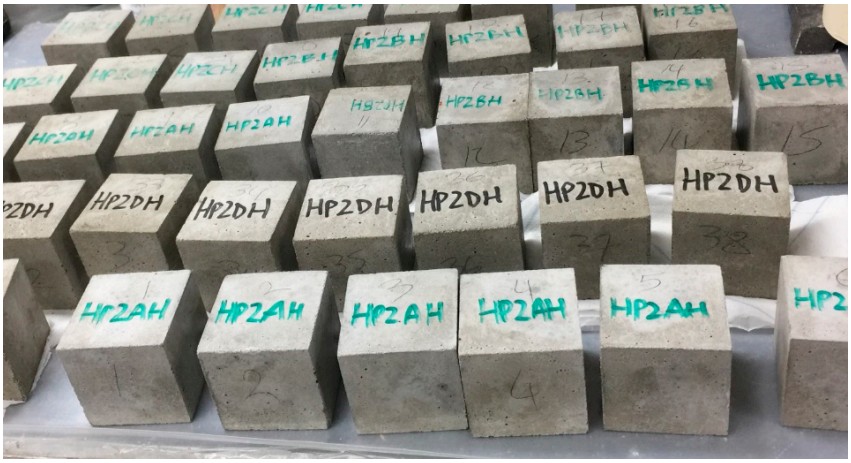

Figure 2. Image of 70 mm cubic backfill mortar samples prepared for acid-resistant evaluation.

2.2.2. Resistivity Measurement

A Proceq four-probe concrete surface resistivity meter was used to measure the resistivity of 100 mm × 200 mm cylindrical mortar samples. The resistivity measurements were taken at 3, 7, 14, 21, 28 and 56 days of curing. To eliminate potential measurement errors due to lime-curing, the resistivity meter was calibrated using standard conversion factors.

2.2.3. Accelerated Testing Regime

The accelerated testing involved immersing the mortar samples in HCl solutions with two different concentrations, 5% and 15% by weight, for up to 28 days. These concentrations were selected to represent a moderate and an aggressive acidification

environment, respectively, reflecting the potential severity of ICCP-induced deterioration observed in the field. A detailed discussion of the HCl concentration considerations is presented in Section 3.1. The acid bath concentrations were monitored and maintained in accordance with the titration protocol as mentioned in Section 2.1.2. After 28 days of standard moist curing, the specimens were immersed under the controlled conditions (23 °C, 50% RH) until testing.

2.2.4. Compressive Strength

The compressive strength of the cubic mortar samples was measured at different curing ages (1 to 56 days) and after certain acid immersion periods (7, 14, and 28 days), following AS 1012.9 [46], using a Controls Sercomp 7 universal testing machine. Two samples from each mix were subjected to compressive strength testing. The samples were loaded at 20 ± 2 MPa per minute until failure.

2.2.5. Gravimetric and Dimensional Analysis

Weight loss and dimensional changes in the acid-immersed cube samples were measured at 7, 14 and 28 days, respectively. Three cube samples from each mix were measured at each immersion period to evaluate their resistance to HCl solutions. Weight measurements were conducted using an electronic scale with an accuracy of 0.1 g. Before immersing the cube samples in acid, the 28-day cured cube samples were immersed in freshwater overnight. They were then dried with paper towels and left at room temperature for two hours to allow surface moisture to evaporate. The weight measurements of the cube samples were taken, serving as the initial weights before acid immersion. For each immersion period, three cube samples were removed from the acid solutions, rinsed with fresh water to remove loose reaction products, and then dried following the same procedure mentioned earlier before weight measurements. After completing the weight and dimensional measurements, one cube sample was sliced to measure the acid diffusion (deterioration) depth, while the remaining two cube samples were tested for compressive strength.

2.2.6. Microstructural Analysis

Microstructural characterisation of the backfill mortars was carried out using XRD, SEM-EDS, and X-ray mapping techniques. Phase identification was performed via powder XRD (Bruker D8 Advance, CuKα radiation, 2θ: 5–90°), using the ICDD PDF database. Morphological and elemental analyses were conducted using SEM-EDS (Hitachi FlexSEM II, 20 keV, low vacuum), while elemental distribution was examined through X-ray mapping (JEOL JSM-7001F FEG-SEM, 15 keV, high vacuum) on polished, carbon-coated samples. Detailed procedures for the microstructural experiments are the same as outlined in Section 2.1.3.

3. Results and Discussion

3.1. Microstructural Comparison Between Field-Exposed and Lab-Controlled Mortar

To assess the acidification mechanisms affecting ICCP anode backfill mortar, a comparative analysis was conducted between samples exposed in the field (deteriorated areas A1 and A2) and laboratory-controlled specimens (HB-40) subjected to 10% and 32.5% HCl immersion regimes. This section investigates the resulting microstructural and mineralogical investigation using XRD, SEM-backscattered electrons (BSE), EDS, and XRM.

The XRD diffractograms of the HB-40 control sample and the bridge pier deteriorated areas A1 and A2 (det. A1 and A2) are presented in Figure 3. The XRD diffractogram of the HB-40 control sample shows that portlandite ($Ca(OH)_2$, PDF#78-0315), ettringite ($Ca_6Al_2(SO_4)_3(OH)_{12}\cdot 26H_2O$, PDF#13-0350), calcium silicate hydrate ($1.5CaO\cdot SiO_2\cdot xH_2O$,

PDF#33-0306) and gypsum ($CaSO_4 \cdot 2H_2O$, PDF#06-0046) are the main hydration phases. Quartz (SiO_2, PDF#33-1161), calcite ($CaCO_3$, PDF#72-1652), vaterite ($CaCO_3$, PDF#24−0030), mullite ($Al_{4.5}Si_{1.5}O_{9.75}$, PDF#82-0037), brownmillerite ($Ca_4Al_2Fe_2^{3+}O_{10}$, PDF#11−0124), and calcium magnesium aluminium oxide silicate ($54CaO \cdot 16SiO_2 \cdot Al_2O_3 \cdot MgO$, PDF#13−0272) are the main crystalline phases in the HB-40.

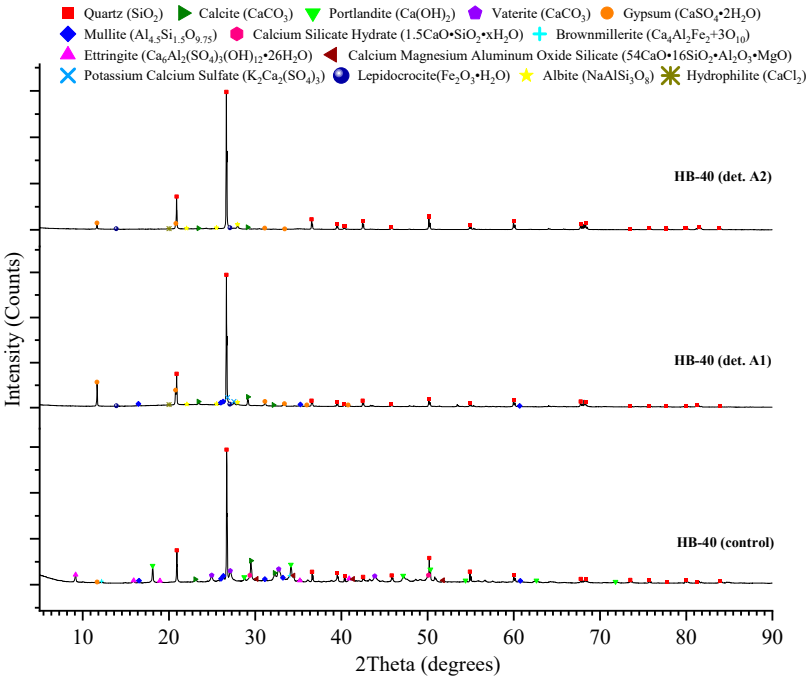

Figure 3. XRD diffractograms of the backfill mortar det. A1 and A2 of the bridge pier sample, compared to the control sample HB-40.

In contrast, the diffractograms of the det. A1 and A2 show partial to full dissolution of most calcium- and aluminium-bearing phases, except for gypsum, whose intensity increased markedly. Additionally, new phases were detected, including lepidocrocite ($Fe_2O_3 \cdot H_2O$, PDF#01−0136), hydrophilite ($CaCl_2$, PDF#12−0056) and potassium calcium sulphate ($K_2Ca_2(SO_4)_3$, PDF#17−0741). The $CaCl_2$ phase was identified in the deteriorated areas, but with low intensities due to its high solubility in water [20]. It should be noted that lepidocrocite is commonly represented as γ-FeO(OH). The presence of $CaCl_2$ and γ-FeO(OH) indicates advanced deterioration of the backfill mortar, in which acidification and chloride ingress have dissolved cement hydration products and initiated reinforcement corrosion.

The degradation mechanisms of ICCP anode backfill mortar are complex, involving both ICCP-induced acidification and seawater-induced chloride and sulphate attack, along with other reactions such as carbonation [47]. Seawater contains approximately 3.4% dissolved salts, primarily sodium and magnesium chlorides and sulphates [48]. The ingress of Cl^- and SO_4^{2-} lowers the pH of the pore solution, increasing the solubility of portlandite (CH), calcium silicate hydrate (C-S-H) and ettringite (AFt). As pH decreases, calcium ions (Ca^{2+}) leach from the matrix, enlarging pores and increasing permeability [49]. In the presence of sufficient SO_4^{2-}, gypsum forms, contributing to internal expansion, cracking and eventual spalling [47,48]. These problems worsen as the anode backfill mortar deteriorates, weakening the surface layer and allowing easy ingress of Cl^-, which attacks the steel reinforcement and causes corrosion.

These findings are supported by SEM-BSE micrographs (Figure 4), which reveal the pore microstructures and formation of gypsum and lepidocrocite crystals within the matrix. These observations are consistent with the findings of Lamond and Pielert [47]

and Hewlett and Liska [48]. Further evidence is provided by XRM in Figure 4, showing the deteriorated bridge anode backfill mortar sample. The pseudo-coloured map reveals the local concentrations of Ca (blue), S (green) and Cl (red), with the combined presence of Ca and S appearing as turquoise. This indicates the formation of gypsum following the dissolution of hydration products. These observations are consistent with the results obtained from the XRD analyses and SEM-BSE micrographs.

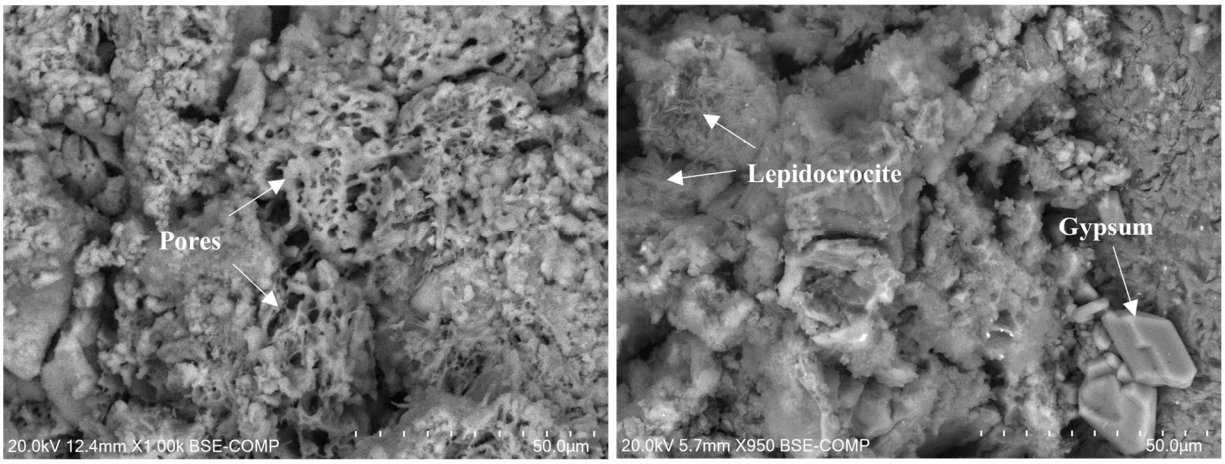

Figure 4. SEM-BSE micrographs of the bridge deteriorated anode backfill mortar sample.

Figure 5d–j EDS maps showing the local distribution of Cl, Ca, Al, Si, S, Fe and Na, respectively. These EDS maps are displayed in grayscale, where brighter colours represent higher concentrations of the respective elements. The maps show Cl^- and SO_4^{2-} migrating inward, while Ca^{2+} and Si^{4+} are leached, consistent with acidification-induced phase dissolution. Around aggregates, gypsum formation likely causes expansion via crystal growth, generating internal stress, cracks and spalling. The EDS maps (Figure 5d,i) show Fe accumulation in Cl-rich zones, suggesting corrosion of steel reinforcement. Migration of corrosion products into the mortar matrix is consistent with XRD and SEM-BSE findings.

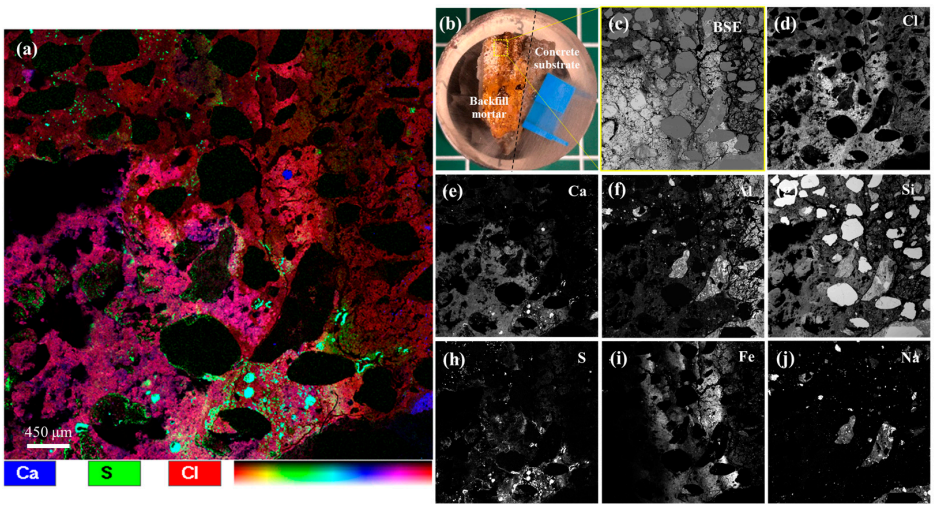

Figure 5. XRM of the deteriorated bridge anode backfill mortar sample: (**a**) pseudo-coloured map revealing local concentrations of Ca (blue), S (green) and Cl (red); (**b**) polished resin-impregnated cross-section of the mortar, with the yellow boxed region indicating the mapped region; (**c**) SEM-BSE micrograph of the yellow boxed region; (**d**–**j**) EDS maps showing the local distribution of Cl, Ca, Al, Si, S, Fe and Na, respectively.

Figure 6 shows XRD diffractograms of HB-40 deteriorated layers exposed to 10% and 32.5% HCl solutions for 28 days. It should be noted that quartz sand was partially removed

from the deteriorated layers using a 1.18 mm sieve to obtain binder-rich samples. Compared to the control, both acid-exposed samples show substantial reduction in calcium- and aluminium-bearing phases, with significant gypsum peak growth, indicating dissolution and reprecipitation processes. Notably, the 10% HCl exposure resulted in a higher gypsum peak intensity than the 32.5% HCl, potentially due to greater Cl^- penetration promoting gypsum precipitation. Further analysis is provided in a later Section 3.2.5.

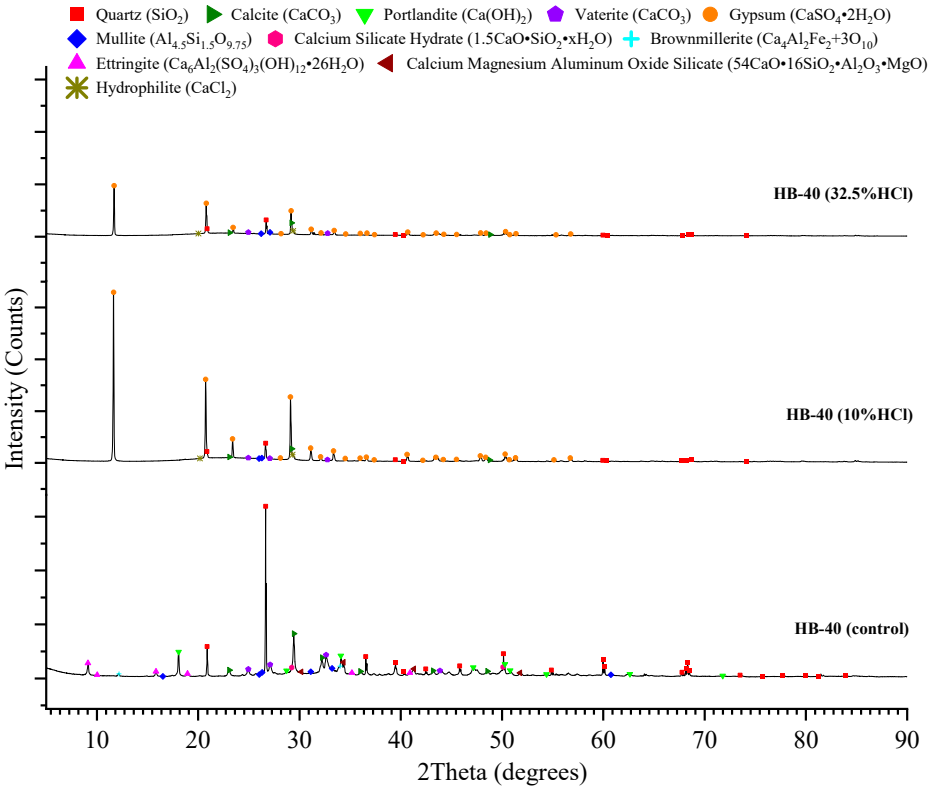

Figure 6. XRD diffractograms of the HB-40 deteriorated layers exposed to HCl solutions for 28 days, compared to the control sample.

A comparison between the field-exposed and laboratory-accelerated samples reveals similar degradation patterns, notably the dissolution of CH, C-S-H and AFt phases, which promotes gypsum formation. However, the laboratory-accelerated regime does not include seawater-induced salts, which may influence longer-term durability mechanisms differently. The HCl solutions used in the laboratory present a more aggressive environment than seawater, primarily due to their lower pH. An amorphous gel-like residue was also observed in the HB-40 samples immersed in HCl solutions after seven days, as shown in Figure 7. This residual is likely silica gel, based on its appearance, consistency, and the expected rapid decalcification of C-S-H under strong acid attack. The formation of such amorphous, gel-like silica has been reported as a characteristic product of C-S-H degradation in acidic environments [50]. The gypsum peak intensity in HCl-exposed samples exceeded that observed in the field samples, consistent with the more severe chemical conditions.

While the current HCl immersion regime presents a more aggressive chemical environment than typical field conditions and does not fully represent other degradation mechanisms, such as seawater-induced sulphate attack or carbonation, it nonetheless provides valuable insight into the fundamental processes of ICCP-related acidification, particularly the dissolution and transformation of cementitious phases. In the next stage of this study, lower HCl concentrations of 5% and 15% are used to approximate the local pH conditions expected near the anode and backfill mortar interface during long-term ICCP exposure, while maintaining an accelerated degradation regime. These concentrations are

not intended to represent bulk pore solution chemistry but instead serve as conservative upper-bound chemical conditions reflecting cumulative local acidification that may develop over extended ICCP service.

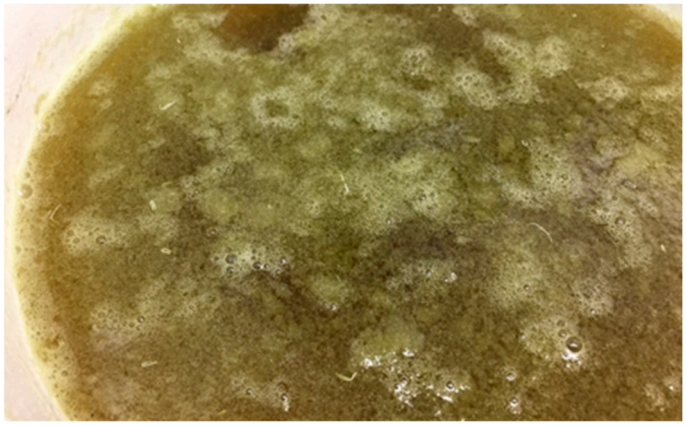

Figure 7. Amorphous gel-like residue was observed in the HB-40 samples immersed in HCl solutions after 7 days of immersion.

The selection of these concentrations is further supported by our previous studies [13,38], which show that oxidation reactions occur at the anode and the backfill mortar interface. In the presence of Cl^-, chlorine gas is generated and subsequently reacts with water to produce HClO and HCl. These reactions progressively lower local pH and induce dissolution and decalcification consistent with the degradation patterns observed under HCl immersion. While the laboratory immersion regime introduces a substantially higher acid dose than would occur during normal ICCP operation, it provides a practical accelerated method for examining long-term deterioration. Conceptually, the severity of attack can be related to the cumulative charge passed at the anode, with extended ICCP service gradually consuming OH^- and generating acid at the interface. Although exact service-time equivalence cannot be determined due to limited field data, the acid dose applied in the immersion tests is broadly representative of the cumulative chemical effects that may develop over several years of ICCP operation. Consequently, the results offer qualitative insight into long-term degradation trends and can inform durability assessment and design.

3.2. Evaluation of Novel Hybrid Backfill Mortars

3.2.1. Resistivity Behaviour

Resistivity reflects the microstructure of backfill mortars by measuring ionic flow between anodic and cathodic regions [51]. According to the American Association of Highway and Transport Officials (AASHTO) T358-15 [52] and Concrete Society Technical Report 60 [51], a value of resistivity above 20 kΩ·cm corresponds to relatively low corrosion rates and reduced chloride ion penetration.

Table 2 presents the resistivity values of the HP-1, HP-2, and HP-3 backfill mortar groups at different curing intervals. The results show that resistivity increased significantly over time, with all samples reaching the 20 kΩ·cm thresholds after 14 days of curing. This highlights the beneficial effect of incorporating SCMs into the backfill mortars, as higher SCMs content generally results in increased resistivity and, in turn, lower corrosion rate in the absence of cathodic protection. In contrast, high-resistivity backfill mortars are not suitable for ICCP applications. These findings align with those of Dodds et al. [51], who reported that samples containing SCMs exhibited resistivity values three to five times higher than those of the reference sample.

Table 2. Resistivity of backfill mortars at different curing intervals.

No. Days	HP-1A	HP-1B	HP-1C	HP-1D	HP-2A	HP-2B	HP-2C	HP-2D	HP-3A	HP-3B	HP-3C	HP-4D
3	2.1	6.3	6.9	7.2	3.2	3.4	2.9	2.9	3.1	3.1	3.1	3.4
7	10.6	11.9	12	13.1	11.7	13.3	11.3	12.8	10.6	10.9	12.8	14.4
14	34.3	39.6	37.8	39.2	19.6	22.1	21.8	24	18.9	20	23.7	26
21	56.3	68.1	64.7	67.5	25.1	27.4	30.2	34.7	24.4	27.1	34.3	34
28	74	88.5	85.8	91.3	28.6	32.1	36.6	37.4	27.9	32.9	38.3	40.6
56	116.4	127.5	116.1	124.8	38.2	42	55	62.2	35	42.2	55.6	60

Unit (kΩ·cm).

Among the groups, the HP-1 group showed significantly higher resistivity, ranging from 116.4 to 127.5 kΩ·cm, which can be attributed to its higher quartz sand content. The HP-2 and HP-3 groups showed similar resistivity values, ranging from 38.2 to 62.2 kΩ·cm and 35 to 60 kΩ·cm, respectively. Except for the HP-1 group, both the HP-2 and HP-3 groups met the requirements specified in AS 2832.5 [16] for anode backfill mortars, maintaining resistivity values below 100 kΩ.cm.

3.2.2. Compressive Strength Development

The strength development of anode backfill mortars (HP-1, HP-2 and HP-3 groups) is compared in Figure 8. All the samples exhibited an increase in strength over time. For the HP-1 group, the compressive strength (f_c') reached 58.1–67.1 MPa at 28 days. After 56 days of curing, HP-1A and HP-1B surpassed 70 MPa, while HP-1C and HP-1D surpassed 60 MPa.

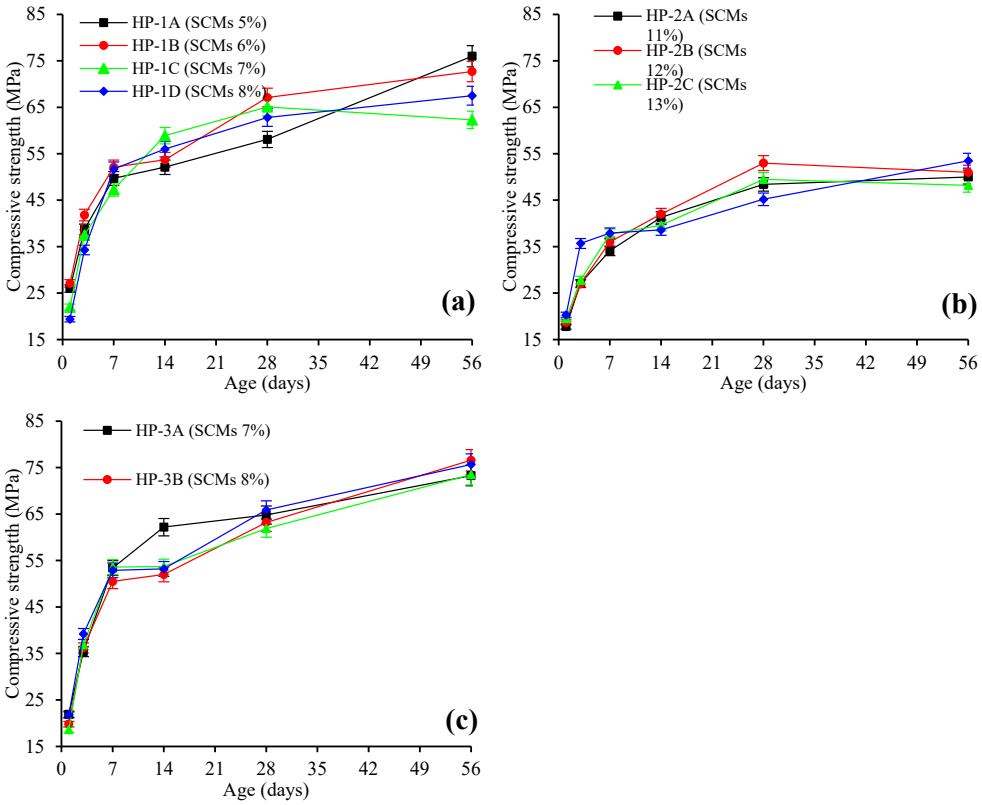

Figure 8. Compressive strength development of backfill mortars with curing time: (**a**) HP-1 group, (**b**) HP-2 group, and (**c**) HP-3 group.

Compared to the HP-1 group, the compressive strength of the HP-2 group decreased by 22.5–29.6%, primarily due to the higher water content. The compressive strengths ranged from 48.2 to 53.5 MPa, with HP-2D exhibiting the highest strength and HP-2C showing the lowest strength within the group. The HP-3 group exhibited a similar trend in

strength development to the HP-1 and HP-2 groups; however, the variation in compressive strength is relatively small. The HP-3 group achieved the highest overall compressive strength, ranging from 73.5 to 76.6 MPa.

3.2.3. Behaviour in HCl Solutions

Loss of Compressive Strength

Figure 9 presents compressive strength loss of HP-1, HP-2 and HP-3 backfill mortar groups after 28-day immersion in 5% and 15% HCl solutions. As shown, the HP-1 group exhibited the greatest susceptibility to acid attack, with compressive strength reductions of 65–78% in 5% HCl solution and 90–93% in 15% HCl solution. Within this group, HP-1C experienced the most severe degradation, showing losses of 78% and 91% in the 5% and 15% HCl solutions, respectively.

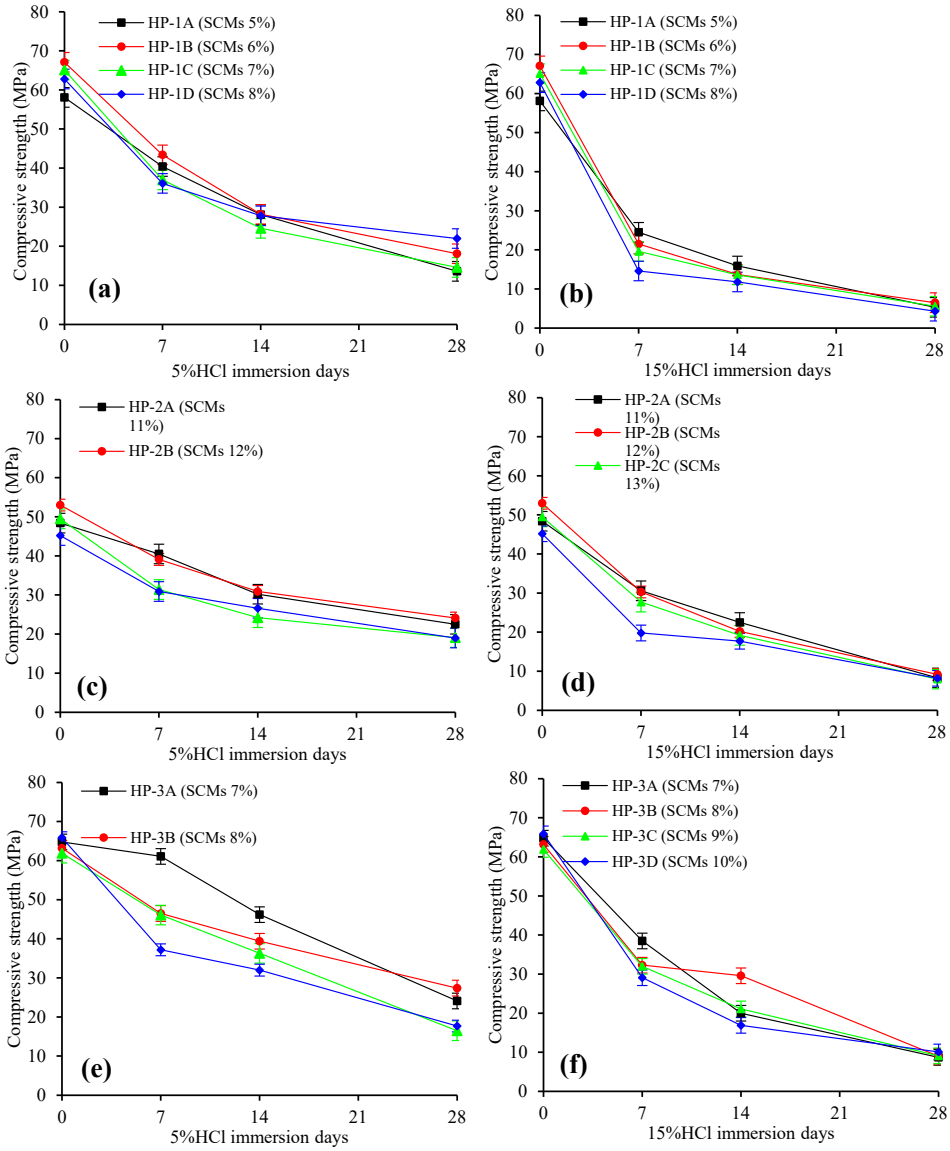

Figure 9. Compressive strength losses of backfill mortars immersed in HCl solutions: (**a**,**b**) HP-1 group, (**c**,**d**) HP-2 group, and (**e**,**f**) HP-3 group.

In contrast, the HP-2 and HP-3 groups demonstrated substantially lower compressive strength losses. This improved performance is attributed to their higher SCMs content, the incorporation of CSA cement, and their lower w/b ratios (0.31 for HP-2 and 0.33 for HP-3, compared to 0.39 for HP-1). Based on the overall trends, the overall order of increasing acid

resistance is HP-2 > HP-3 > HP-1. Notably, HP-2A exhibited the least degradation, with strength losses of 54% in 5% HCl solution and 83% in 15% HCl solution.

A comparison with HB-40 Plus (HB-40 modified by replacing 25–40 wt.% OPC with GGBS), a Portland cement-based acid-resistant mortar, further contextualises these results. HB-40 Plus exhibited an average resistivity of 162 kΩ·cm, a typical 28-day compressive strength of 50.0 MPa, and compressive strength reductions of 61% and 78% after 28 days of immersion in 5% and 15% HCl solutions, respectively. In the 5% HCl solution, the HP-1 and HP-3 groups experienced slightly greater strength loss than HB-40 Plus, whereas the HP-2 group showed comparable or lower reductions. In contrast, at the 15% HCl solution, HB-40 Plus displayed less strength loss than all HP-1, HP-2 and HP-3 groups. Overall, HP-2 and HP-3 groups exhibited degradation levels broadly comparable to HB-40 Plus, indicating that these hybrid mortars can perform at a level similar to that of the acid-resistant mortars.

These findings are consistent with expectations, as SCMs can enhance concrete durability in aggressive chemical environments [25]. The incorporation of SCMs such as GGBS, fly ash and silica fume improves the chemical resistance of mortars compared with mortars solely containing OPC [53,54]. SCMs typically contain higher Si and lower Ca contents than OPC [31]. Under acidic environments (pH 3–5), Ca-rich phases dissolve more readily than Si- or Al-rich phases; consequently, Ca leaches rapidly, while Si tends to form a protective $SiO_2 \cdot nH_2O$ gel layer that slows further degradation [50]. Furthermore, both SCMs and CSA cement reduce the $Ca(OH)_2$ content in the cement matrix, making mortars with high SCMs and CSA contents less vulnerable to acid-induced deterioration [32,55].

Mass Loss

Table 3 presents the percentage mass loss of HP-1, HP-2 and HP-3 backfill mortar groups after immersion in 5% and 15% HCl solutions for up to 28 days. In both acid concentrations, mass loss increased consistently with longer exposure time. In the 5% HCl solution, HP-3A exhibited the lowest mass loss among all mixes, recording 1.4% at 7 days, 2.8% at 14 days and 4.9% at 28 days. In contrast, the other mixes experienced higher mass loss at 28 days, ranging from 5% to 7.2%. For the 15% HCl solution, HP-3B showed the least degradation, with a 28-day mass loss of 7.2%. HP-1D exhibited the highest mass loss at 28 days, reaching 27.4%, while the remaining mixes recorded mass losses between 8.7% and 15.9%. Overall, the HP-2 and HP-3 groups demonstrated relatively lower mass loss compared to the HP-1 group, particularly under the higher acid concentrations. This improved resistance is attributed to the higher content of SCMs and the incorporation of CSA cement in the HP-2 and HP-3 groups.

Table 3. Mass loss of backfill mortars immersed in HCl solutions.

HCl%	No. Days	HP-1A	HP-1B	HP-1C	HP-1D	HP-2A	HP-2B	HP-2C	HP-2D	HP-3A	HP-3B	HP-3C	HP-4D
5	7	3	2.3	3.5	3.4	0.6	1.6	3	2.7	1.4	1.8	2.1	3.5
	14	3.3	3	5.8	4	3.4	4.6	6.8	6.5	2.8	4.3	5.1	6.7
	28	5.7	5	6.9	6	5	5.8	7	6.9	4.9	5.9	6	7.2
15	7	6.1	9.3	11.2	17.3	4.2	5.1	5.7	6.5	4.3	5.2	5.6	5.6
	14	12.9	14.1	13.2	19.8	-	10.8	8.1	9.7	6.4	6.4	8.5	9
	28	13.1	14.5	15.9	27.4	12.1	11	12.6	12.4	10.9	7.2	8.7	10.5

Unit (per cent).

Deterioration Depth

Table 4 presents the deterioration depth of backfill mortars HP-1, HP-2 and HP-3 groups after immersion in 5% and 15% HCl solutions for 28 days. As shown in Figure 10, the deterioration depth of all mixes increased with both longer exposure duration and higher acid concentrations. In the 5% HCl solution, the HP-2 and HP-3 groups exhibited lower deterioration depths than the HP-1 group. This improved resistance is attributed to

their higher SCMs contents (11–14 wt.% for HP-2 group and 7–10 wt.% for HP-3 group), as SCMs contribute to a denser matrix, reducing permeability, and lower $Ca(OH)_2$ content in the cement system [56].

Table 4. Deterioration depth of backfill mortars.

HCl%	No. Days	HP-1A	HP-1B	HP-1C	HP-1D	HP-2A	HP-2B	HP-2C	HP-2D	HP-3A	HP-3B	HP-3C	HP-4D
5	7	1	1.5	2.5	3	1	1.5	1.5	1.5	0.8	1	1.5	2
	14	3	4	4	-	2	3	3	3	2	-	3	4
	28	6	6	6	6	3	4	5	5	3	3	5	5
15	7	3	4	4	4.5	2	2.5	4	4	2	3	3	4
	14	7	7	7	7	5	5	6	6	5	5	6	6
	28	8	8	9	9	8.5	8.5	9	9	9	9	10	10

Unit (mm).

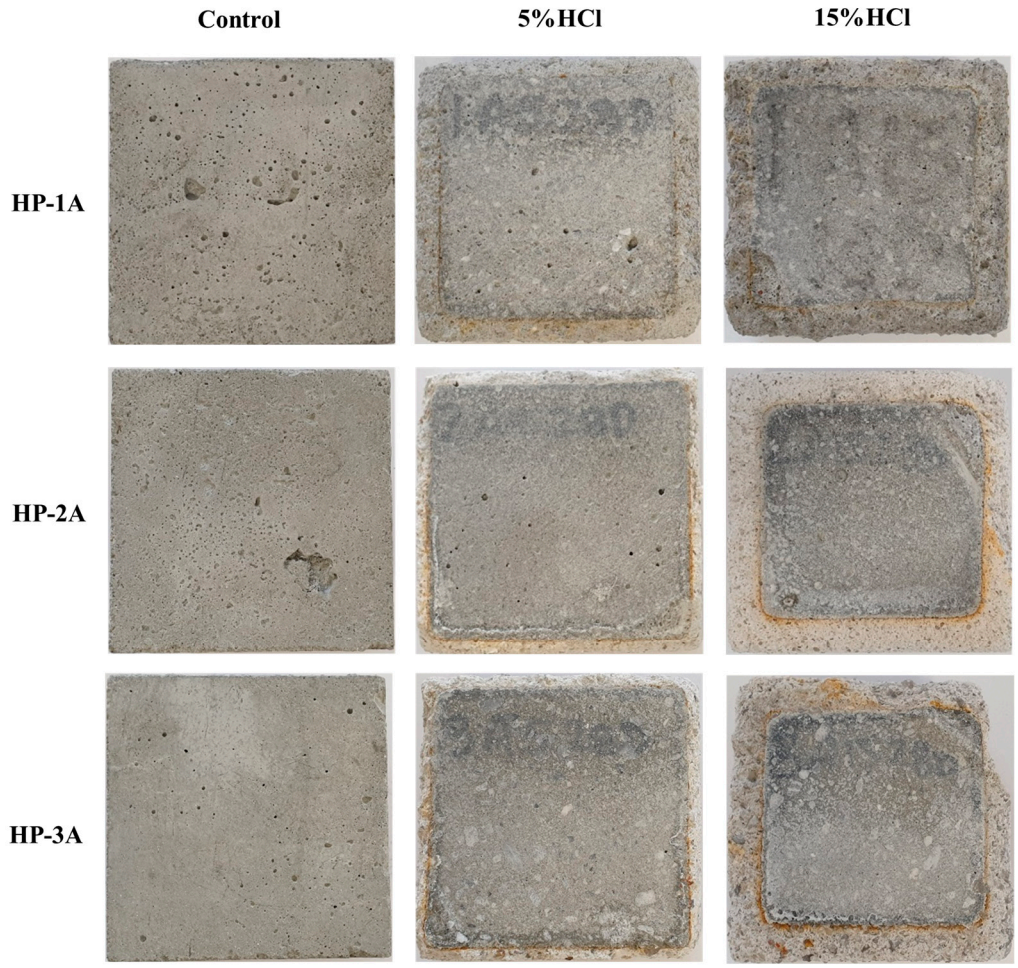

Figure 10. Transverse sections of control and 28-day HCl solutions immersed backfill mortars HP-1A, HP-2A and HP-3A.

A similar trend was observed in the 15% HCl solution at 14 days, where HP-2 and HP-3 groups again showed lower deterioration depths than the HP-1 group at 14 days. However, at 28 days, this trend reversed, with the HP-1 group showing lower deterioration depths than both the HP-2 and HP-3 groups. This unexpected reversal may be related to variations in sample permeability or other microstructural differences, indicating that further investigation is needed to fully identify the mechanisms responsible for these discrepancies.

3.2.4. Practical Implications

Table 5 summarises the practical implications of the backfill mortars under different acidification scenarios to guide the selection of suitable backfill materials. It identifies which mortar types perform better under moderate (5% HCl solution) and aggressive (15% HCl solution) exposure conditions based on a combined assessment of electrical resistivity and acid-resistance indicators, including compressive strength retention, mass loss, and deterioration depth.

Table 5. Combined performance assessment of backfill mortars.

Mix ID	Resistivity kΩ·cm	Moderate 5% HCl				Aggressive 15% HCl			
		SR [1] %	Mass Loss %	DD [2] mm	Score	SR [1] %	Mass Loss %	DD [2] mm	Score
HP-2A	38.2	46	5	3	11	17	12.1	8.5	16
HP-2B	42	45	5.8	4	13	17	11	8.5	14
HP-2C	55	39	7	5	19	16	12.6	9	17
HP-2D	62.2	42	6.9	5	14	18	12.4	9	11
HP-3A	35	37	4.9	3	16	13	10.9	9	19
HP-3B	42.2	43	5.9	3	13	14	7.2	9	13
HP-3C	55.6	27	6	5	18	15	8.7	10	12
HP-3D	60	27	7.2	5	20	15	10.5	10	12

[1] SR = Compressive strength retention; [2] DD = Deterioration depth.

As discussed in Section 3.2.1, only the HP-2 and HP-3 groups satisfy the resistivity requirement for anode backfill mortars, maintaining values below 100 kΩ·cm. Each performance indicator was individually ranked on a scale from 1 to 8, where 1 represents the best performance and 8 the poorest. The rankings were then summed to determine the overall performance score for each exposure scenario. Under moderate exposure, HP-2A is the preferred option, as it exhibits the lowest combined performance score of 11. Under aggressive exposure, HP-2D is recommended for the same reason, having the most favourable overall score among all tested mortars.

This ranking approach may assist designers and engineers in selecting durable anode backfill mortars for varying acidification risks.

3.2.5. Microstructural Analysis

XRD Analysis

The XRD diffractograms of the backfill mortars (HP-1A, HP-2A and HP-3A) from both control and deteriorated layers exposed to 5% and 15% HCl solutions are presented in Figures 11–13. To enrich the binder fraction in the deteriorated samples, quartz sand was partially removed using a 1.18 mm sieve before XRD analysis. Figure 11 shows the diffractograms of backfill mortar HP-1A, where several hydration products such as portlandite ($Ca(OH)_2$, PDF#78-0315), gypsum ($CaSO_4{\cdot}2H_2O$, PDF#06-0046), calcium aluminium hydrate ($Ca_4Al_2O_7{\cdot}13H_2O$, PDF#11-0203), tobermorite ($4CaO{\cdot}5SiO_2{\cdot}5H_2O$, PDF#03-0239), ettringite ($Ca_6Al_2(SO_4)_3(OH)_{12}{\cdot}26H_2O$, PDF#13-0350), and hydrotalcite ($Mg_{0.667}Al_{0.333}(OH)_2(CO_3)_{0.167}(H_2O)_{0.5}$, PDF#89-0460) were identified. These hydration phases govern the physical and chemical properties of the hybrid backfill mortar system. In addition, quartz (SiO_2, PDF#33-1161), calcite ($CaCO_3$, PDF#72-1652), larnite (Ca_2SiO_4, PDF#83-0460), mullite ($Al_{4.5}Si_{1.5}O_{9.75}$, PDF#82-0037), thenardite (Na_2SO_4, PDF#01-1009), and brownmillerite ($Ca_4Al_2\ Fe_2^{3+}O_{10}$, PDF#11-0124) were also identified.

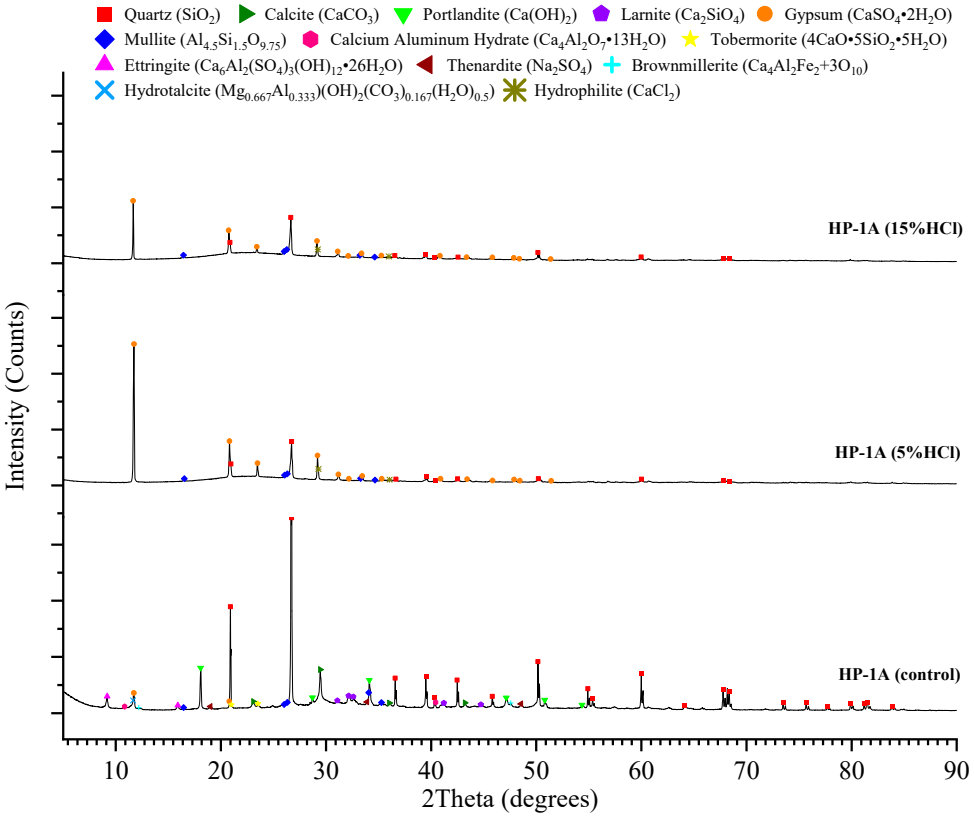

Figure 11. XRD diffractograms of the HP-1A control and the deteriorated layers exposed to HCl solutions for 28 days.

In the deteriorated layer, however, most calcium- and aluminium-bearing hydration products were completely dissolved, except for the gypsum, which exhibited a significant increase in peak intensity. The increase suggests the formation of secondary gypsum as a reaction product of leached Ca^{2+} and SO_4^{2-} under acidic conditions. Notably, the 5% HCl-exposed sample showed higher gypsum peak intensities than the one exposed to 15% HCl solution, despite the latter being more acidic. This may be attributed to enhanced ion diffusion at lower HCl concentrations, which promoted Ca^{2+} leaching and subsequent gypsum precipitation.

The ingress of Cl^- and hydrogen ions (H^+) from the HCl solution initiated the breakdown of the cement matrix. These ions lowered the pore solution pH, neutralising the alkalinity and dissolving primary hydration products such as CH and C-S-H [57,58]. This process released Ca^{2+}, which reacted with SO_4^{2-} to form gypsum [18,30]. The availability of SO_4^{2-} and leached Ca^{2+} influenced gypsum formation. SO_4^{2-} showed a stronger tendency for binding with hydration products compared to Cl^- ($SO_4^{2-} > Cl^- > OH^-$), thereby promoting gypsum formation [59]. The XRD diffractograms also showed the presence of amorphous silica, visible as a broad hump in the 2θ range of 20 to 30°, which results from the breakdown of C-S-H under strong acid attack [60].

The progression of phase dissolution follows the thermodynamic model proposed by Hemstad et al. [58], where CH dissolves first, followed by C-S-H, AFt, and then hydrotalcite. The dissolution process gives rise to the formation of secondary phases, including gypsum, amorphous silica and hydrophilite ($CaCl_2$, PDF#12-0056), further indicating severe chemical degradation.

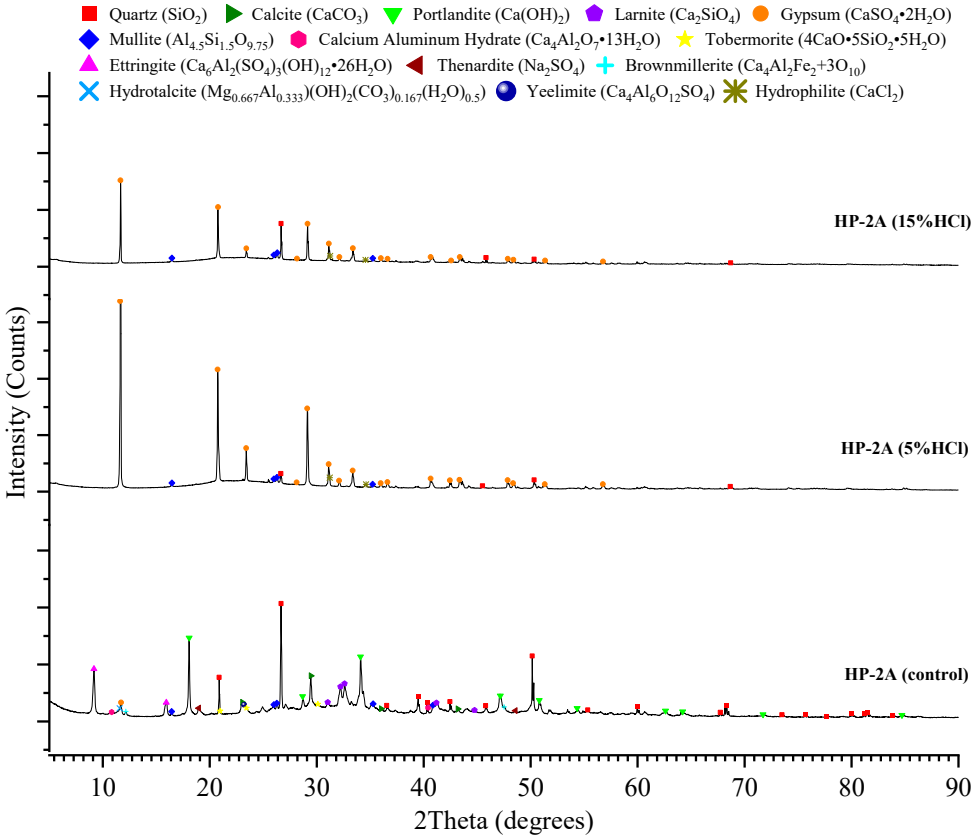

Figure 12. XRD diffractograms of the HP-2A control and the deteriorated layers exposed to HCl solutions for 28 days.

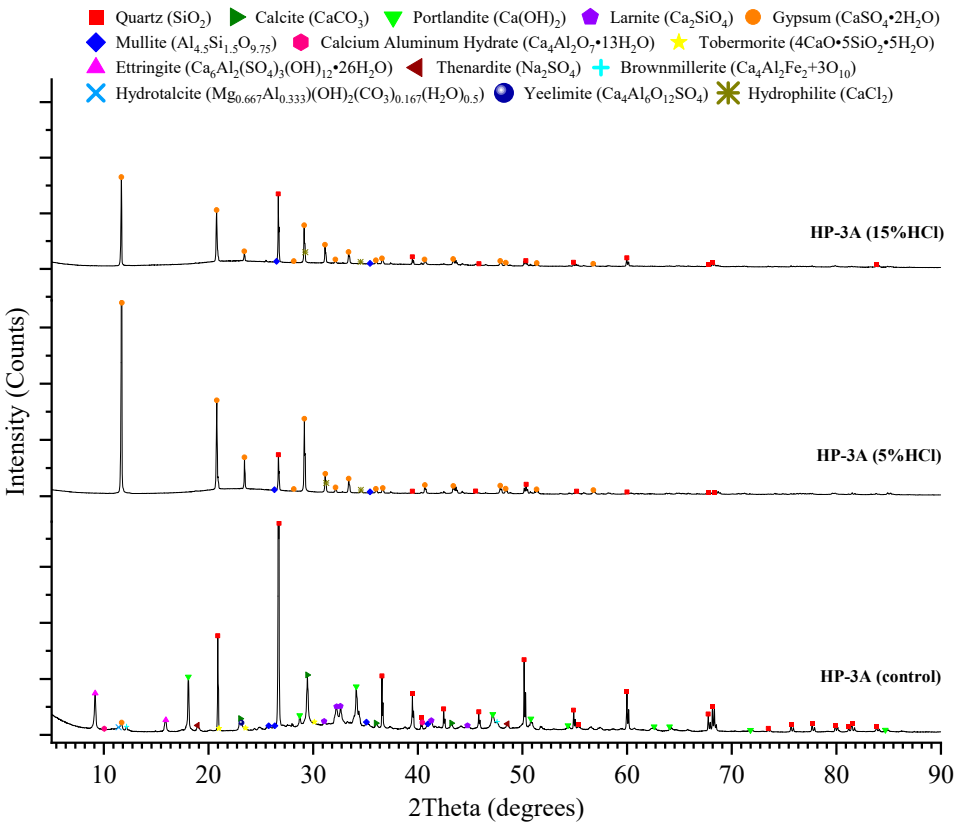

Figure 13. XRD diffractograms of the HP-3A control and the deteriorated layers exposed to HCl for 28 days.

Similar phase changes were observed in HP-2A and HP-3A (Figures 12 and 13). In both cases, the control samples showed comparable hydration products, with additional presence of ye'elimite ($Ca_4Al_6O_{12}SO_4$, PDF#33-0256), which was attributed to the incorporation of CSA cement in these mixes. Ye'elimite is the primary hydration product of the CSA cement system [34]. Upon exposure to HCl solutions, the deteriorated layers of HP-2A and HP-3A also showed significant dissolution of calcium- and aluminium-bearing phases, with the formation of gypsum, amorphous silica and $CaCl_2$. Notably, the intensity of gypsum peaks in HP-2A and HP-3A deteriorated layers exceeded those of HP-1A, suggesting more extensive gypsum formation. This could be attributed to the additional dissolution of AFt and ye'elimite, both of which release Ca^{2+} and $SO_4{}^{2-}$ upon breakdown, further facilitating gypsum crystallisation [32].

The chemical phase transformations revealed by XRD explain the mechanical degradation trends observed earlier. The progressive dissolution of binding phases such as CH, C-S-H and AFt correlates directly with the observed losses in compressive strength, particularly the HP-1 group, which exhibited up to 93% strength loss in 15% HCl-exposure. This weakening of the matrix is further supported by the increased mass loss and deterioration depth over the 28-day immersion period.

The formation of gypsum, while initially densifying the matrix, likely contributed to microstructural cracking and expansion over time. Despite this, the HP-2 and HP-3 groups exhibited relatively lower mass loss and deterioration depth, demonstrating the effectiveness of CSA cement in mitigating acid attack. Although volume stability was not directly assessed in this study, further investigation is required to clarify the long-term effects of gypsum-induced expansion. Additionally, the presence of amorphous silica and $CaCl_2$, both indicative of advanced degradation, aligns with the observed loss of matrix cohesion and increasing porosity.

SEM-EDS Analysis

The oxide compositions of the backfill mortars (HP-1A, HP-2A and HP-3A) in both the control and the deteriorated layers following exposure to HCl solutions are summarised in Table 6. SEM-EDS analysis was used to investigate the microstructural and chemical changes in these layers. For each sample, five regions were analysed at a magnification of hundred times (100×). The primary elements detected in all backfill mortars were Ca, Si and Al. In the control samples, Ca content was considerably higher in the deteriorated layers, confirming that acid exposure led to the dissolution and leaching of Ca^{2+} from the cement matrix into the surrounding solution [48]. These findings align with the XRD analysis, which showed significant losses of calcium-bearing hydration products, such as CH, C-S-H and AFt, in the degraded zones. The decrease in Ca and Al concentrations, along with the relative increase in Si, suggests that Si-rich phases remained intact in the deteriorated layer, possibly forming a gel-like amorphous silica barrier that inhibits further acid ingress. This is supported by the presence of broad humps in the 2θ range of 20 to 30° in the XRD diffractograms, characteristic of amorphous silica [50].

In addition, the trace elements such as Fe, Mg and Na also showed reduced concentrations in the deteriorated layers, indicating their dissolution and subsequent leaching into the acid solution. Conversely, the concentration of S increased significantly in the degraded zones. This increase can be attributed to the dissolution of sulphate-bearing phases, such as AFt and ye'elimite, and the subsequent formation of gypsum [58]. Figure 14 shows the morphology and elemental composition of gypsum crystals formed in the deteriorated layer, consistent with the XRD results.

Table 6. Chemical compositions of backfill mortars.

Samples	HCl%	CaO	SiO_2	Al_2O_3	Fe_2O_3	SO_3	MgO	Na_2O	K_2O	TiO_2	Cl
HP-1A control	-	46.76	39.35	6.77	2.52	1.89	1.16	0.59	0.53	0.43	-
HP-1A det. layer	5	12.96	63.33	5.6	0.97	5.23	0.45	0.17	0.6	1.27	9.42
HP-1A det. layer	15	14.01	61.57	5.96	0.74	3.76	0.39	0.2	0.48	0.66	12.23
HP-2A control	-	57.87	23.85	8.97	2.05	4	1.76	0.56	0.5	0.43	-
HP-2A det. layer	5	14.5	59.85	5.44	0.51	13	0.22	0.18	0.35	1.7	4.25
HP-2A det. layer	15	19.15	47.63	5.44	-	10.76	0.33	0.2	0.31	0.8	15.39
HP-3A control	-	57.6	28.17	5.05	2.24	4.28	1.36	0.35	0.43	0.51	-
HP-3A det. layer	5	15.63	59.19	1.54	0.6	16.24	0.18	0.2	0.26	1.52	4.63
HP-3A det. layer	15	20.66	46.6	1.32	-	11.59	0.38	0.39	0.16	0.4	18.49

Unit (% by total mass).

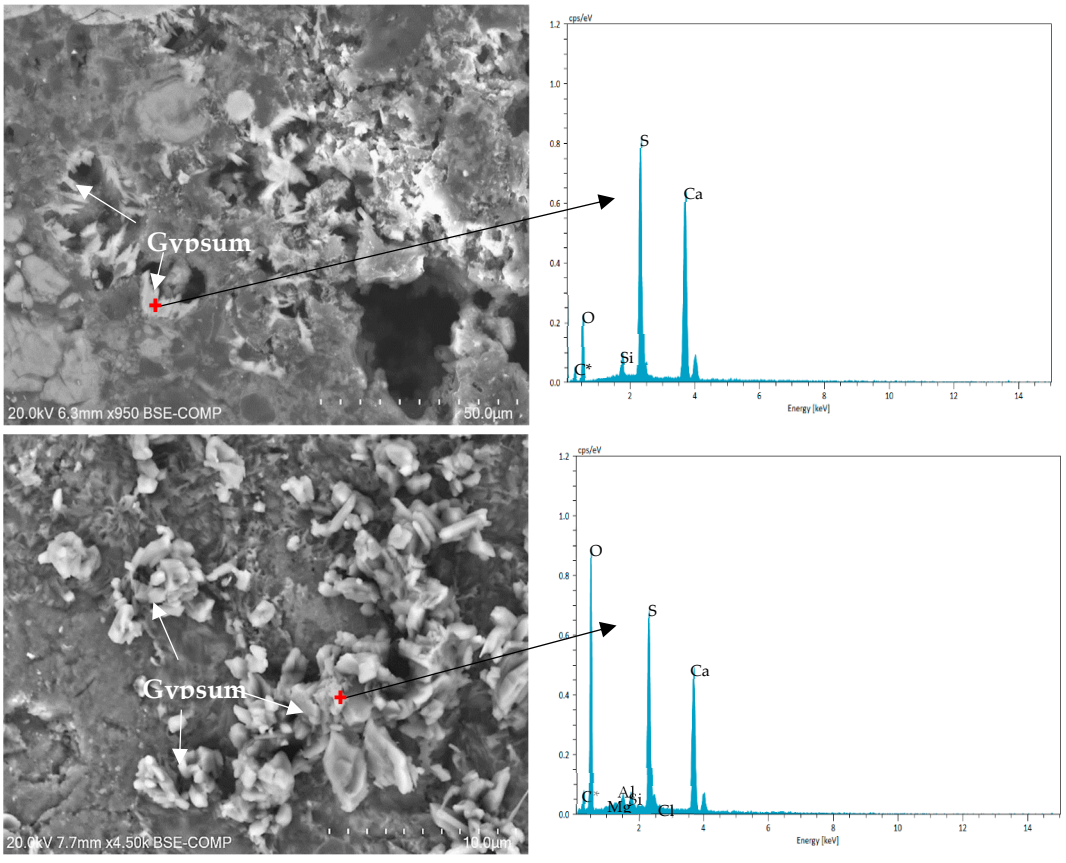

Figure 14. SEM-BSE micrographs and EDS spectra of gypsum in the deteriorated layer of HCl-exposed backfill mortar.

An important aspect revealed by the SEM-EDS analysis was the variation in Cl content across the different acid concentrations. Notably, samples exposed to the 5% HCl solution exhibited lower Cl content in the deteriorated layer compared to those exposed to the 15% HCl solution. This lower Cl content in the 5% HCl-exposed samples can be explained by

several interrelated factors. First, the pH of the external solution does not directly reflect the internal pH of the cement matrix. As Cl^- diffuse inward, they interact with and gradually neutralise the surrounding alkaline pore solution, altering local pH conditions and affecting ion transfer and binding dynamics [61]. Second, while both acid concentrations promote significant dissolution of Ca-rich hydration products such as CH and C-S-H, the more aggressive 15% HCl solution causes more rapid and extensive degradation, leading to higher Cl^- ingress in the matrix. In contrast, under 5% HCl-exposure, slower reaction kinetics and enhanced diffusion may lead to greater Ca^{2+} leaching into the external solution, where it may preferentially form soluble $CaCl_2$ rather than contributing to Cl^- binding within the matrix [61].

Furthermore, the presence of SO_4^{2-}, released from the breakdown of AFt and ye'elimite, introduces an additional level of complexity. SO_4^{2-} has a stronger tendency for binding with hydration products than Cl^-, thereby promoting the formation of gypsum in the deteriorated layer. This competitive binding mechanism may further inhibit Cl^- binding, especially under conditions where gypsum formation is more favourable, such as in the moderately 5% HCl solution [62].

X-Ray Mapping

Figure 15 presents the XRM of the boundary interface between the intact mortar and the deteriorated layer of the sample exposed to the 15% HCl solution. The pseudo-coloured map illustrates the local concentrations of Al (blue), Ca (green) and S (red). The overlapping presence of Ca and S in the region appears as orange, indicating the dissolution of calcium- and sulphate-bearing hydration products and the subsequent formation of gypsum within this zone. This observation is consistent with the earlier findings from the XRD and SEM-EDS analyses, further confirming gypsum precipitation in the deteriorated layer.

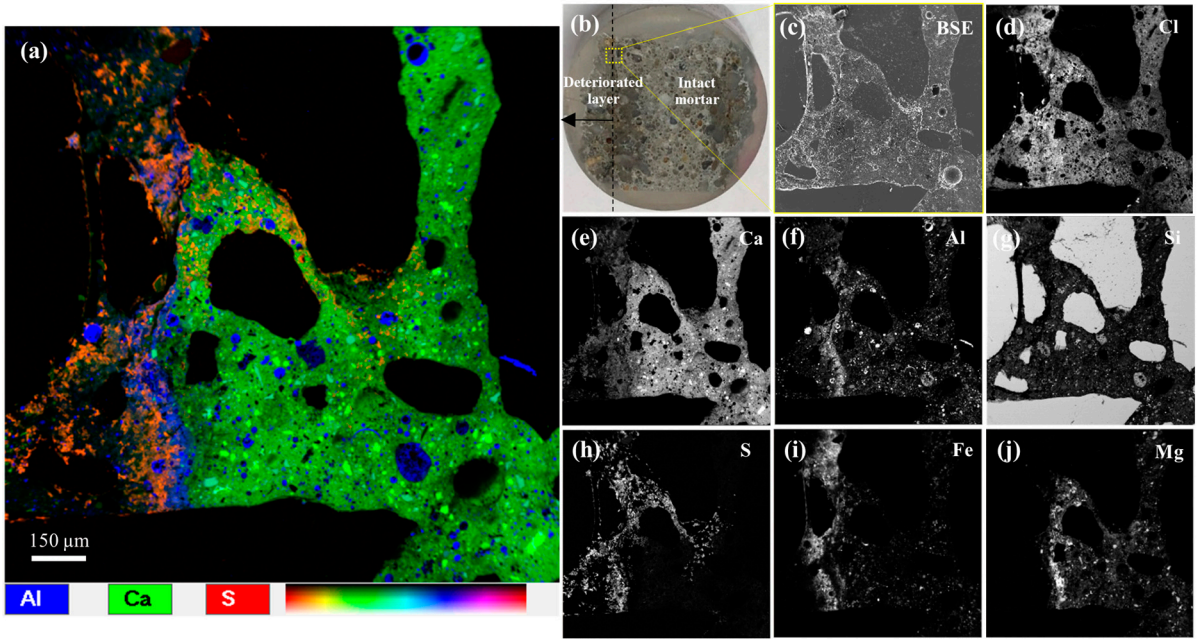

Figure 15. XRM of the boundary interface between the intact mortar and the deteriorated layer exposed to 15% HCl solution: (**a**) pseudo-coloured map revealing local concentrations of Al (blue), Ca (green) and S (red); (**b**) polished resin-impregnated transverse section of the mortar, with the yellow boxed region indicating the mapped region; (**c**) SEM-BSE micrograph of the yellow boxed region; (**d**–**j**) EDS maps showing the local distribution of Cl, Ca, Al, Si, S, Fe and Mg, respectively.

Figure 15d–j EDS maps show the local distribution of Cl, Ca, Al, Si, S, Fe and Mg, respectively. These EDS maps are displayed in grayscale, with brighter colours indicating

higher concentrations of the respective elements. The maps reveal that Ca^{2+}, Al^{3+}, $SO_4{}^{2-}$, Fe^{2+} and Mg^{2+} have migrated from the intact matrix toward the deteriorated layer, suggesting progressive dissolution and outward diffusion. Meanwhile, Cl^- migrated inward from the HCl solution into the mortar. Additionally, Ca^{2+} appeared to diffuse beyond the deteriorated layer and into the external HCl solution, resulting in a reduced Ca concentration within the deteriorated region compared to the intact mortar [63].

This migration and ion exchange process is associated with the progressive neutralisation of pore solution alkalinity in the deteriorated layer. As Ca^{2+}, Al^{3+}, $SO_4{}^{2-}$, Fe^{2+} and Mg^{2+} diffuse outward and Cl^- migrates inward, the ionic equilibrium within the pore solution shifts. To maintain electroneutrality, anions such as OH^- leach out due to the dissolution of hydration phases, particularly CH, C-S-H, AFt, which releases OH^- and $SO_4{}^{2-}$. This mechanism is supported by equilibrium chloride binding experiments and thermodynamic modelling reported by De Weerdt [61]. These processes contributed to a decrease in the pH and the crystallisation of gypsum within the pore structure [20,62]. As the pore solution pH fell below 12, Cl^- binding declined substantially, reaching negligible levels at pH = 9. Furthermore, competition between Cl^- and $SO_4{}^{2-}$ for binding on hydration products further suppressed Cl^- binding capacity [58,62].

These findings provide a microchemical explanation for the reduced compressive strength loss observed in the HP-2 and HP-3 groups compared to the HP-1 group when exposed to HCl solutions. The incorporation of CSA cement in HP-2 and HP-3 groups likely contributed to higher OH^- and $SO_4{}^{2-}$ release during the acid-induced breakdown of AFt and ye'elimite phases. This enhanced the formation of gypsum while simultaneously reducing Cl^- binding within the cement matrix, thereby mitigating acid-induced structural degradation.

4. Conclusions

The acidification of the anode backfill mortar significantly affects the long-term durability and service life of the ICCP system. This study investigated the feasibility of utilising blended cement with CSA cement and zeolite in ICCP anode backfill mortars and evaluated their performance under controlled exposure to varying concentrations of HCl solution. The experimental regime was validated through comparison with field-exposed samples, confirming its effectiveness in simulating key degradation mechanisms relevant to ICCP-induced acidification. Based on the experimental results, the following conclusions can be drawn:

(1) The use of blended cement has a notably beneficial effect on improving resistivity. After a 14-day curing period, all three mortar groups exceeded the minimum resistivity requirement of 20 kΩ·cm, indicating lower corrosion rates and reduced Cl^- penetration in the absence of a cathodic protection system. Furthermore, HP-2 and HP-3 groups remained below the upper limit of 100 kΩ·cm, thereby meeting the performance criteria for ICCP anode backfill mortars and demonstrating the effectiveness of blended cement.

(2) The incorporation of SCMs and CSA cement in backfill mortars enhances their resistance to acid attack, particularly in chloride-rich environments. HP-2 and HP-3 groups exhibited significantly lower compressive strength losses compared to the HP-1 group when exposed to HCl solutions. The HP-2 group showed the least loss, with a 54% reduction at 5% HCl and 83% at 15% HCl. The HP-3 group consistently showed the lowest mass loss and shallower deterioration depths. These results confirm that higher SCM content with CSA cement and zeolite improves acid resistance and mechanical durability, making these mortars more suitable for aggressive service conditions.

(3) Microstructural analyses (XRD, SEM-EDS and XRM) revealed substantial dissolution of calcium- and sulphate-bearing hydration products, ion migration, and the formation of gypsum within the deteriorated layers. The competition interaction between Cl^- and SO_4^{2-} plays a crucial role in reducing Cl^- binding capacity. The presence of CSA cement in the HP-2 and HP-3 groups promoted the greater release of OH^- and SO_4^{2-} during HCl exposure, which enhanced gypsum formation while limiting Cl^- binding. This mechanism contributed to a significantly lower compressive strength loss compared to the HP-1 group.

Overall, backfill mortars with higher SCM content, incorporating CSA cement and zeolite (HP-2 and HP-3 groups), demonstrated outstanding acid resistance and mechanical durability compared to the HP-1group. Microstructural analyses confirmed that gypsum formation and chloride–sulphate interactions critically influence degradation mechanisms, underpinning the improved durability of these hybrid mortars in corrosive environments.

Author Contributions: H.F.: Conceptualisation, Methodology, Validation, Resources, Writing—review & editing, Supervision, Project administration, Funding acquisition. S.A.H.: Validation, Resources, Writing—review & editing, Visualisation, Supervision, Project administration. G.A.: Methodology, Validation, Investigation. S.S.: Software, Validation, Investigation, Data Curation. Q.H.: Methodology, Software, Validation, Formal analysis, Investigation, Data Curation, Writing—original draft, Visualisation. M.M.: Validation, Investigation. Y.T.: Writing—review & editing, Visualisation. All authors have read and agreed to the published version of the manuscript.

Funding: This research was funded by the Australian Research Council's Discovery Early Career Researcher Award (DECRA) fellowship scheme (project DE200100406), as well as by the University of Sydney—National University of Singapore Ignition Grants.

Data Availability Statement: The data presented in this study are available on request from the corresponding author.

Acknowledgments: The authors would like to thank the Faculty of Engineering, University of Sydney, Parchem for Construction Supplies Pty Ltd., and the Advanced Materials Characterisation Facility (AMCF) of Western Sydney University for their collaboration on this research project. Hadigheh would like to acknowledge the support he received from the Australian Government through the Australian Research Council's Discovery Early Career Researcher Award (DECRA) fellowship scheme (project DE200100406), as well as from the University of Sydney—National University of Singapore Ignition Grants. Special thanks are given to Richard Wuhrer, Laurel George and Daniel Fanna from AMCF at Western Sydney University.

Conflicts of Interest: Author Georgius Adam and Michael McKinnon was employed by the company Dulux Group Pty Ltd. The remaining authors declare that the research was conducted in the absence of any commercial or financial relationships that could be construed as a potential conflict of interest.

References

1. Hu, J.; Wang, Y.; Zhang, Z.; Guo, W.; Ma, Y.; Zhu, W.; Wei, J.; Yu, Q. Evaluation on the acidification damage of the external anode mortar induced by impressed current cathodic protection. *Constr. Build. Mater.* **2019**, *229*, 116869. [CrossRef]
2. Machello, C.; Bazli, M.; Rajabipour, A.; Hadigheh, S.A.; Rad, H.M.; Arashpour, M.; Hassanli, R. FRP bar and concrete bond durability in seawater: A meta-analysis review on degradation process, effective parameters, and predictive models. *Structures* **2024**, *62*, 106231. [CrossRef]
3. Liu, P.; Tang, J.-P.; Feng, R.; Fan, Y.; Zhu, J.-H. Interfacial behaviour and shear performance of polarized CFRCM-strengthened corroded RC continuous beams. *Constr. Build. Mater.* **2025**, *472*, 140786. [CrossRef]
4. Wang, B.; Wang, Z.; Uji, K.; Zhang, J.; Guo, R. Experimental investigation on shear behavior of RC beams strengthened by CFRP grids and PCM. *Structures* **2020**, *27*, 1994–2010. [CrossRef]
5. Liu, P.; Tang, J.-P.; Feng, R.; Fan, Y.; Zhu, J.-H. Tensile behavior and flexural performance of polarized CFRCM-strengthened corroded RC continuous beams. *Structures* **2025**, *76*, 109022. [CrossRef]

6. Carmona, J.; Garcés, P.; Climent, M.A. Efficiency of a conductive cement-based anodic system for the application of cathodic protection, cathodic prevention and electrochemical chloride extraction to control corrosion in reinforced concrete structures. *Corros. Sci.* **2015**, *96*, 102–111. [CrossRef]
7. Wilson, K.; Jawed, M.; Ngala, V. The selection and use of cathodic protection systems for the repair of reinforced concrete structures. *Constr. Build. Mater.* **2013**, *39*, 19–25. [CrossRef]
8. Hou, L.; Feng, R.; Huang, Y.; Xu, Y.; Zhu, J.-H. Compressive behavior of seawater sea sand concrete (SSC) composite columns with dual-functional C-FRCM jacket under eccentric loading. *Constr. Build. Mater.* **2025**, *502*, 144450. [CrossRef]
9. Stratfull, R.F. Experimental cathodic protection of a bridge deck. *Transp. Res. Rec.* **1974**, *500*, 1–15.
10. Pourbeix, M. Atlas of electrochemical equilibria in aqueous solution. *Corros. Sci.* **1966**, *10*, 343.
11. Christodoulou, C.; Glass, G.; Webb, J.; Austin, S.; Goodier, C. Assessing the long term benefits of Impressed Current Cathodic Protection. *Corros. Sci.* **2010**, *52*, 2671–2679. [CrossRef]
12. Christodoulou, C.; Sharifi, A.; Das, S.; Goodier, C. Cathodic protection on the UK's Midland Links motorway viaducts. In Proceedings of the Institution of Civil Engineers-Bridge Engineering, London, UK, 2 June 2014; pp. 43–53. [CrossRef]
13. Fatemi, H.; Hadigheh, S.A.; Tao, Y.; Adam, G. Development of a novel and specialised cementitious matrix overlay for anode embedment in impressed current cathodic protection (ICCP) systems for reinforced concrete bridges. *Case Stud. Constr. Mater.* **2024**, *20*, e02908. [CrossRef]
14. Broomfield, J.P. An overview of cathodic protection criteria for steel in atmospherically exposed concrete. *Corros. Eng. Sci. Technol.* **2020**, *55*, 303–310. [CrossRef]
15. Goyal, A.; Pouya, H.S.; Ganjian, E.; Claisse, P. A review of corrosion and protection of steel in concrete. *Arab. J. Sci. Eng.* **2018**, *43*, 5035–5055. [CrossRef]
16. *AS 2832.5—2008*; Cathodic Protection of Metals Part 5: Steel in Concrete Structures. Standards Australia: Sydney, Australia, 2008.
17. Elsener, B. Long-term durability of electrochemical chloride extraction. *Mater. Corros.* **2008**, *59*, 91–97. [CrossRef]
18. Hu, J.; Wang, Y.; Ma, Y.; Wei, J.; Yu, Q. Identification on acidification damage of external anode system induced by impressed current cathodic protection for reinforced concrete. *Math. Biosci. Eng.* **2019**, *16*, 7510–7525. [CrossRef] [PubMed]
19. Koleva, D.A.; de Wit, J.H.W.; van Breugel, K.; Veleva, L.P.; van Westing, E.; Copuroglu, O.; Fraaij, A.L.A. Correlation of microstructure, electrical properties and electrochemical phenomena in reinforced mortar. Breakdown to multi-phase interface structures. Part II: Pore network, electrical properties and electrochemical response. *Mater. Charact.* **2008**, *59*, 801–815. [CrossRef]
20. Alnahhal, M.F.; Alengaram, U.J.; Jumaat, M.Z.; Alsubari, B.; Alqedra, M.A.; Mo, K.H. Effect of aggressive chemicals on durability and microstructure properties of concrete containing crushed new concrete aggregate and non-traditional supplementary cementitious materials. *Constr. Build. Mater.* **2018**, *163*, 482–495. [CrossRef]
21. Zhang, E.Q.; Abbas, Z.; Tang, L. Predicting degradation of the anode–concrete interface for impressed current cathodic protection in concrete. *Constr. Build. Mater.* **2018**, *185*, 57–68. [CrossRef]
22. Soomro, M.; Tam, V.W.Y.; Jorge Evangelista, A.C. 2-Production of cement and its environmental impact. In *Recycled Concrete*; Tam, V.W.Y., Soomro, M., Jorge Evangelista, A.C., Eds.; Woodhead Publishing: Cambridge, UK, 2023; pp. 11–46. [CrossRef]
23. Saleh, H.M.; Eskander, S.B. 18-Innovative cement-based materials for environmental protection and restoration. In *New Materials in Civil Engineering*; Samui, P., Kim, D., Iyer, N.R., Chaudhary, S., Eds.; Butterworth-Heinemann: Oxford, UK, 2020; pp. 613–641. [CrossRef]
24. Neupane, K.; Hadigheh, S.A. Sodium hydroxide-free geopolymer binder for prestressed concrete applications. *Constr. Build. Mater.* **2021**, *293*, 123397. [CrossRef]
25. Mlinárik, L.; Kopecskó, K. The influence of combined application of two SCMs on the corrosion and acid attack durability of mortars. *Period. Polytech. Civ. Eng.* **2017**, *61*, 313–321. [CrossRef]
26. Saraswathy, V.; Song, H.-W. Evaluation of corrosion resistance of Portland pozzolana cement and fly ash blended cements in pre-cracked reinforced concrete slabs under accelerated testing conditions. *Mater. Chem. Phys.* **2007**, *104*, 356–361. [CrossRef]
27. Le, D.-H.; Sheen, Y.-N.; Lam, M.N.-T. Fresh and hardened properties of self-compacting concrete with sugarcane bagasse ash–slag blended cement. *Constr. Build. Mater.* **2018**, *185*, 138–147. [CrossRef]
28. Wang, Z.; Zeng, Q.; Wang, L.; Yao, Y.; Li, K. Characterizing blended cement pastes under cyclic freeze–thaw actions by electrical resistivity. *Constr. Build. Mater.* **2013**, *44*, 477–486. [CrossRef]
29. Ram, K.; Serdar, M.; Londono-Zuluaga, D.; Scrivener, K. The effect of pore microstructure on strength and chloride ingress in blended cement based on low kaolin clay. *Case Stud. Constr. Mater.* **2022**, *17*, e01242. [CrossRef]
30. Noushini, A.; Castel, A. The effect of heat-curing on transport properties of low-calcium fly ash-based geopolymer concrete. *Constr. Build. Mater.* **2016**, *112*, 464–477. [CrossRef]
31. Liao, Y.; Cai, Z.; Deng, F.; Ye, J.; Wang, K.; Tang, S. Hydration behavior and thermodynamic modelling of ferroaluminate cement blended with steel slag. *J. Build. Eng.* **2024**, *97*, 110833. [CrossRef]
32. Damion, T.; Cepuritis, R.; Chaunsali, P. Sulfuric acid and citric acid attack of calcium sulfoaluminate-based binders. *Cem. Concr. Compos.* **2022**, *130*, 104524. [CrossRef]

33. Kriptavičius, D.; Girskas, G.; Skripkiūnas, G. Use of Natural Zeolite and Glass Powder Mixture as Partial Replacement of Portland Cement: The Effect on Hydration, Properties and Porosity. *Materials* **2022**, *15*, 4219. [CrossRef] [PubMed]
34. Tambara, L.U.D.; Cheriaf, M.; Rocha, J.C.; Palomo, A.; Fernández-Jiménez, A. Effect of alkalis content on calcium sulfoaluminate (CSA) cement hydration. *Cem. Concr. Res.* **2020**, *128*, 105953. [CrossRef]
35. Mehta, A.; Siddique, R. Sulfuric acid resistance of fly ash based geopolymer concrete. *Constr. Build. Mater.* **2017**, *146*, 136–143. [CrossRef]
36. Ariffin, M.; Bhutta, M.; Hussin, M.; Tahir, M.M.; Aziah, N. Sulfuric acid resistance of blended ash geopolymer concrete. *Constr. Build. Mater.* **2013**, *43*, 80–86. [CrossRef]
37. Domingos, L.; Azevedo, A.; Lombardi, C.; Strecker, K. Corrosion resistance of fly ash-based geopolymer in hydrochloric and sulfuric acid solutions. *Cerâmica* **2020**, *66*, 394–403. [CrossRef]
38. Hadigheh, S.A.; Ke, F.; Fatemi, H. Durability design criteria for the hybrid carbon fibre reinforced polymer (CFRP)-reinforced geopolymer concrete bridges. *Structures* **2022**, *35*, 325–339. [CrossRef]
39. Vafaei, M.; Allahverdi, A.; Dong, P.; Bassim, N. Acid attack on geopolymer cement mortar based on waste-glass powder and calcium aluminate cement at mild concentration. *Constr. Build. Mater.* **2018**, *193*, 363–372. [CrossRef]
40. Zainal, F.F.; Kamarudin, H.; Rahmat, A.; Abdullah, M.M.A.B.; Rizam, S.; Selimin, M.T.; Sandu, A.V. The electrical resistivity of geopolymer paste by using Wenner four probe method. *Key Eng. Mater.* **2015**, *660*, 28–33. [CrossRef]
41. Ali, M.; Jenkins, G.; Bird, A. Swansea Bridge cathodic protection works. In Proceedings of the 8th Austroads Bridge Conference 2011, Sydney, NSW, Australia, 31 October–5 November 2011.
42. Berger, I.; Healy, D.; Tilley, M. Movable span bridges of NSW: A new classification system. In Proceedings of the 9th Austroads Bridge Conference, Sydney, NSW, Australia, 22–24 October 2014; pp. 22–24.
43. Fatemi, H.; Hadigheh, A.; Adam, G. Mitigating the risk of acidification in reinforced concrete bridge impressed current cathodic protection systems. In Proceedings of the Austroads Bridge Conference, 11th, 2022, Adelaide, SA, Australia, 15–18 November 2022.
44. FOSROC. Sampling Cement Based Grout-Compressive Strength Testing. 2025. Available online: https://www.fosroc.com.au/sites/default/files/resources_file_storage/Compressive_strength_testing-cement_based_grouts.pdf (accessed on 9 April 2025).
45. *AS 1012.8.3−2014*; Method 8.1: Method for Making and Curing Concrete—Mortar and Grout Specimens. Standard Australia: Sydney, NSW, Australia, 2015.
46. *AS 1012.9−2014*; Method 9: Compressive Strength Tests—Concrete, Mortar and Grout Specimens. Standards Australia: Sydney, NSW, Australia, 2014.
47. Lamond, J.F.; Pielert, J.H. *Significance of Tests and Properties of Concrete and Concrete-Making Materials*; ASTM International: Conshohocken, PA, USA, 2006; Volume 169.
48. Hewlett, P.C.; Liska, M. *Lea's Chemistry of Cement and Concrete*, 5th ed.; Butterworth-Heinemann: Oxford, UK, 2017.
49. Wang, L.; Jin, M.; Zhou, S.; Tang, S.; Lu, X. Investigation of microstructure of C-S-H and micro-mechanics of cement pastes under NH4NO3 dissolution by 29Si MAS NMR and microhardness. *Measurement* **2021**, *185*, 110019. [CrossRef]
50. Shi, C.; Stegemann, J. Acid corrosion resistance of different cementing materials. *Cem. Concr. Res.* **2000**, *30*, 803–808. [CrossRef]
51. Dodds, W.; Goodier, C.; Christodoulou, C.; Austin, S.; Dunne, D. Corrosion risk assessment of structural concrete with coarse crushed concrete aggregate. *Proc. Inst. Civ. Eng.-Constr. Mater.* **2020**, *173*, 57–69. [CrossRef]
52. *T358-15*; Standard Test Method for Surface Resistivity Indication of Concretes Ability to Resist Chloride Ion Penetration. American Association of State Highway and Transport Officials (AASHTO): Washington, DC, USA, 2015.
53. Tao, Y.; Hadigheh, S. Electrochemical performance and corrosion mitigation of steel-embedded cementitious composites with recycled carbon fibre and CFRP composites in accelerated marine conditions. *Electrochim. Acta* **2025**, *548*, 148004. [CrossRef]
54. Roy, D.; Arjunan, P.; Silsbee, M. Effect of silica fume, metakaolin, and low-calcium fly ash on chemical resistance of concrete. *Cem. Concr. Res.* **2001**, *31*, 1809–1813. [CrossRef]
55. Lothenbach, B.; Scrivener, K.; Hooton, R.D. Supplementary cementitious materials. *Cem. Concr. Res.* **2011**, *41*, 1244–1256. [CrossRef]
56. O'Connell, M.; McNally, C.; Richardson, M.G. Performance of concrete incorporating GGBS in aggressive wastewater environments. *Constr. Build. Mater.* **2012**, *27*, 368–374. [CrossRef]
57. Tritthart, J. Chloride binding in cement II. The influence of the hydroxide concentration in the pore solution of hardened cement paste on chloride binding. *Cem. Concr. Res.* **1989**, *19*, 683–691. [CrossRef]
58. Hemstad, P.; Machner, A.; De Weerdt, K. The effect of artificial leaching with HCl on chloride binding in ordinary Portland cement paste. *Cem. Concr. Res.* **2020**, *130*, 105976. [CrossRef]
59. Pargar, F.; Koleva, D.A.; Van Breugel, K. Determination of Chloride Content in Cementitious Materials: From Fundamental Aspects to Application of Ag/AgCl Chloride Sensors. *Sensors* **2017**, *17*, 2482. [CrossRef]
60. Mourhly, A.; Khachani, M.; Hamidi, A.E.; Kacimi, M.; Halim, M.; Arsalane, S. The Synthesis and Characterization of Low-Cost Mesoporous Silica SiO2 from Local Pumice Rock. *Nanomater. Nanotechnol.* **2015**, *5*, 35. [CrossRef]

61. De Weerdt, K. Chloride binding in concrete: Recent investigations and recognised knowledge gaps: RILEM Robert L'Hermite Medal Paper 2021. *Mater. Struct.* **2021**, *54*, 214. [CrossRef]
62. Jain, A.; Gencturk, B.; Pirbazari, M.; Dawood, M.; Belarbi, A.; Sohail, M.G.; Kahraman, R. Influence of pH on chloride binding isotherms for cement paste and its components. *Cem. Concr. Res.* **2021**, *143*, 106378. [CrossRef]
63. Pavlik, V. Corrosion of hardened cement paste by acetic and nitric acids Part III: Influence of water/cement ratio. *Cem. Concr. Res.* **1996**, *26*, 475–490. [CrossRef]

Disclaimer/Publisher's Note: The statements, opinions and data contained in all publications are solely those of the individual author(s) and contributor(s) and not of MDPI and/or the editor(s). MDPI and/or the editor(s) disclaim responsibility for any injury to people or property resulting from any ideas, methods, instructions or products referred to in the content.